



City Research Online

City, University of London Institutional Repository

Citation: Nykteri, G. & Gavaises, M. (2022). Numerical modelling of droplet rim fragmentation by laser-pulse impact using a multiscale two-fluid approach. *Physical Review Fluids*, 7(10), 103604. doi: 10.1103/PhysRevFluids.7.103604

This is the accepted version of the paper.

This version of the publication may differ from the final published version.

Permanent repository link: <https://openaccess.city.ac.uk/id/eprint/28943/>

Link to published version: <https://doi.org/10.1103/PhysRevFluids.7.103604>

Copyright: City Research Online aims to make research outputs of City, University of London available to a wider audience. Copyright and Moral Rights remain with the author(s) and/or copyright holders. URLs from City Research Online may be freely distributed and linked to.

Reuse: Copies of full items can be used for personal research or study, educational, or not-for-profit purposes without prior permission or charge. Provided that the authors, title and full bibliographic details are credited, a hyperlink and/or URL is given for the original metadata page and the content is not changed in any way.

City Research Online:

<http://openaccess.city.ac.uk/>

publications@city.ac.uk

1 Numerical modelling of droplet rim fragmentation 2 by laser-pulse impact using a multiscale two-fluid approach

3 Georgia Nykteri and Manolis Gavaises

4 *School of Mathematics, Computer Science & Engineering, Department of Mechanical Engineering & Aeronautics,*
5 *City University of London, Northampton Square EC1V 0HB, United Kingdom*

7 **Abstract**

8 The present work examines the rim fragmentation of a millimeter-sized methyl-ethyl-ketone (MEK)
9 droplet imposed by the impact of different millijoule nanosecond laser beams that correspond to
10 droplet propulsion velocity values between 1.76 m/s and 5.09 m/s. The numerical investigation is
11 conducted within a physically consistent and computationally efficient multiscale framework, using
12 the Σ -Y two-fluid model with dynamic local topology detection. Overall, the macroscopic droplet
13 expansion and the obtained deforming shape show good agreement with the experimental
14 observations. The influence of the laser beam energy on the droplet deformation and the evolution
15 of the detached fragments from the rim is demonstrated. The physical mechanisms that determine
16 the droplet expansion, including the expansion velocity and expansion rate, along with the effect of
17 the surrounding air flow on the detached fragments, are addressed. Despite the visualization
18 limitations inside the polydisperse cloud of fragments in the experimental results at higher laser
19 energy, the evolution of fragments during the fragmentation process is quantified for the first time,
20 and size distributions are obtained within the multiscale framework.

21 **Keywords:** laser impact, droplet fragmentation, rim breakup, two-fluid model, multiscale model

22 **1. Introduction**

23 The droplet response to a laser-pulse impact is a polyparametric phenomenon, which remains of
24 primary significance in varied state-of-the-art applications of both industrial and medical interest,
25 including, among others, the extreme ultra-violent (EUV) light emission in lithography
26 machines [1], [2], [3], [4], the micromachining in the fabrication of photonic devices [5], [6], [7] and
27 the laser ablation of biological tissues [8], [9], [10], [11]. The absorption of the laser energy by the
28 liquid droplet results in rapid and explosive phase-change phenomena, such as cavitation [12], [13],
29 vaporization [14], [15], [16], and plasma formation [17], [18], observed in both transparent and liquid
30 metal droplets. As a consequence of the developed droplet dynamics after the laser-pulse impact, the
31 droplet moves, deforms, and fragments into different patterns, dependent on the intensity of the
32 applied laser beam energy and the material of the liquid droplet.

33 Several experimental studies in the literature investigate the laser-imposed fragmentation of a liquid
34 droplet under different experimental configurations, which as a result, lead to different post-impact
35 mechanisms. In the early literature, Kafalas & Herrmann [14] and Kafalas & Ferdinand [15] examined
36 the explosive vaporization of single micron-sized water droplets imposed by a pulsed CO₂ laser with
37 an energy of approximately 0.5 J per pulse. Later, Pinnick et al. [19] extended the explosive
38 vaporisation study for different liquids, e.g. for ethanol and diesel droplets, and observed similar
39 fragmentation patterns with the water experiments for a pulsed CO₂ laser and comparable energy.
40 Similar explosive response was also observed for micron-sized liquid metal droplets in the experiments
41 of Basko et al. [20] and Grigoryev et al. [21]; in this case, the picosecond laser pulse results in the
42 development of plasma state inside the droplet, while the development and propagation of a GPa
43 pressure pulse inside the droplet triggers the subsequent violent fragmentation. More recently,
44 Gonzalez Avila & Ohl [12] and Zeng et al. [22] studied a different explosive fragmentation mode, which

45 is developing as an outward widespread jetting from the droplet surface. Specifically, the laser impact
46 onto a millimetre-sized water droplet with a cavitation bubble in the centre imposes a laser-induced
47 cavitation and bubble oscillations that penetrate the droplet surface; different fragmentation regimes
48 were identified based on the dynamic pressure and the energy of the expanding bubble. In an attempt
49 to control the deposition of the laser energy inside the droplet, Klein et al. [23], [24], [25] proposed
50 the use of opaque liquid droplets, which restrict the energy absorption in a thin superficial layer on
51 the illuminated side of the droplet. Specifically, Acid-Red-1 and Oil-Red-O solutions were utilized for
52 water and methyl-ethyl-ketone (MEK) droplets, respectively, in order to investigate the droplet
53 response to a broad range of laser energy between 1 mJ and 420 mJ. Additionally, the similarities
54 between the physical principles that govern the laser-induced droplet fragmentation and the
55 fragmentation due to the mechanical impact of a droplet onto a solid surface [26] were highlighted;
56 the impulsive acceleration of the droplet due to the laser impact can be correlated with the impulsive
57 deceleration of the droplet when impacting the solid. Recently, Rao et al. [27] demonstrated the
58 influence of the laser focus and energy on the resulting fragmentation of an array of micron-sized
59 water and diesel droplets and identified a new butterfly type fragmentation pattern. Overall, the
60 available experimental studies in the literature provide a thorough analysis of the droplet dynamics
61 and the physical mechanisms that govern the subsequent fragmentation. However, due to the
62 multiscale character of the fragmentation process, very few quantitative data are available regarding
63 the produced fragments, for instance in the high resolution experimental visualizations of Klein et
64 al. [25] and Rao et al. [27], which mainly concern moderate fragmentation regimes.

65 The hydrodynamics response of a liquid droplet to a laser-pulse impact is driven by the imposed recoil
66 pressure on the droplet surface, as discussed in previous analytical and numerical studies in the
67 literature. Specifically, the smooth particle hydrodynamics (SPH) method is commonly adopted for the
68 investigation of liquid tin droplets, which are subject to high energy picosecond laser beams. As
69 depicted in the works of Grigoryev et al. [21] and Koukouvinis et al. [28], the SPH method can
70 accurately predict the recoil pressure establishment and propagation inside the droplet, shortly after
71 the laser-pulse impact, the formation of dominant cavitation regions, and the early-time explosive
72 fragmentation, using a given particles population. Concerning the commonly utilized Eulerian
73 methods in droplet fragmentation simulations due to mechanical impact [29], [30], [31], Zeng et
74 al. [22] employed the Volume of Fluids (VOF) method to study the cavitation-induced liquid jetting of
75 a water droplet with a gas bubble in the centre at initial conditions, impacted by a millijoule laser
76 pulse. The coherent droplet interface and the formation of multiple outward liquid jets were
77 accurately captured with the sharp interface method; however, the small-scaled fragments remain
78 unresolved with the VOF method, which can result in significant loss of information in more violent
79 fragmentation regimes with dominant polydisperse fragments. Gelderblom et al. [32] proposed the
80 boundary integral (BI) method for the simulation of the laser-induced droplet deformation. The BI
81 simulations precisely capture the droplet lateral and width deformation under different conditions;
82 nevertheless, the effects of the surrounding air and the subsequent fragmentation of the elongated
83 liquid sheet were excluded from the numerical modelling. Additionally, Gelderblom et al. [32] and
84 Reijers et al. [33] presented an analytical solution for the developed flow fields inside the droplet,
85 during the early-times of the droplet response to the laser-pulse impact. The analytical studies
86 provided a further insight into the obtained recoil pressure and the resulting droplet dynamics that
87 finally initiate the droplet deformation; however, the analysis is restricted to the early times, before
88 the droplet deformation becomes significant.

89 Following the numerical challenges imposed by the unrevealed laser-induced droplet fragmentation
90 mechanisms, there is a gap in the up-to-date literature regarding a comprehensive numerical analysis
91 that can capture both the early-time droplet dynamics, evolving shortly after the laser-pulse impact

92 and the later-time droplet fragmentation with consideration of all the produced multiscale fragments.
93 The present study proposes the multiscale two-fluid approach, as developed by Nykteri et al. [34], in
94 order to investigate the multiscale character of the later-time droplet fragmentation. The numerical
95 methodology has been previously validated against droplet fragmentation cases, driven by the high-
96 speed mechanical impact on a solid surface [34]. In the present numerical simulations, the multiscale
97 two-fluid approach employs a sharp interface method for the deforming and laterally expanding liquid
98 droplet and a physically consistent sub-grid scale modelling for the produced small-scaled fragments,
99 due to the rim breakup. The novelty of the conducted simulations lies on the thorough quantitative
100 analysis of both the early-time and the later-time droplet dynamics with a viable computational cost.
101 Specifically, significant information regarding the liquid droplet expansion into an elongated liquid
102 sheet is revealed, including the droplet radial expansion velocity and the effect of the surrounding air.
103 Additionally, the influence of the applied laser beam energy is demonstrated and shows good
104 agreement with both the experimental observations of Klein et al. [25] and theory. Finally, for the first
105 time in the up-to-date literature, an overview of the evolution of the produced fragments' population
106 is presented. The fragments dynamics, including the development of a cloud of fragments in the
107 course of the fragmentation process and the interaction between the detached fragments and the
108 surrounding air under the impact of different beams, are highlighted and sizes distributions are
109 obtained.

110 In section 2 are presented all the details of the numerical configuration for the conducted laser-
111 induced droplet fragmentation simulations, including the problem formulation as described in the
112 experimental studies of Klein et al. [23], [24], [25], the early-time dynamics simulations, the governing
113 equations of the multiscale two-fluid approach and the later-time dynamics simulations set-up.
114 Following, in section 3 the numerical investigations for the rim fragmentation of a liquid droplet,
115 imposed by different intensity laser beams are discussed. The numerical results are compared with
116 the experimental observations of Klein et al. [25] for the same examined conditions. Finally, the major
117 conclusions are summarized in section 4.

118 **2. Numerical modelling**

119 The fragmentation of a millimetre-sized methyl-ethyl-ketone (MEK) droplet imposed by the impact of
120 a millijoule nanosecond laser pulse is investigated in the present study using numerical simulations.
121 The MEK droplet with an initial radius of $R_0 = 0.9$ mm, density $\rho = 805$ kg/m³, kinematic viscosity
122 $\nu = 0.53 \times 10^{-6}$ m²/s and surface tension $\gamma = 0.025$ N/m lies in a nitrogen environment at ambient
123 conditions ($p = 1$ atm, $T = 20^\circ$ C). The laser-induced droplet dynamics concern two main stages, namely
124 the early-time droplet response to the laser pulse and the later-time droplet deformation and
125 fragmentation. The early-time droplet dynamics are discussed in §2.1 based on the experimental
126 investigations of Klein et al. [23], [24], [25] and a physically consistent numerical modelling is
127 presented in §2.2, following the analytical model of Gelderblom et al. [32]; the obtained pressure and
128 velocity fields inside the droplet are subsequently utilized for the initialization of the conducted
129 numerical simulations that capture the later-time phenomena. The numerical simulations of the later-
130 time droplet deformation and fragmentation are performed using the multiscale two-fluid approach,
131 presented in §2.3. Details of the simulation set-up are summarized in §2.4.

132 **2.1. Problem formulation**

133 The numerical modelling of the laser-induced droplet fragmentation is based on the problem
134 formulation and the fundamental principles of the early- and later-time droplet dynamics, as
135 introduced in the experimental studies of Klein et al. [23], [24], [25] and illustrated in Figure 1.

136 The early-time droplet dynamics in Figure 1(i-ii) are characterized by the millijoule nanosecond laser
 137 pulse impact onto the droplet that results to local boiling on the superficial layer with thickness
 138 $\delta \ll R_0$ and the emission of a very small vapour mass in the surrounding air. The resulting recoil
 139 pressure on the droplet surface accelerates the droplet, until it finally reaches a constant propulsion
 140 velocity U , as expressed in the momentum conservation below:

$$141 \quad mu = \rho R_0^3 U \quad (1)$$

142 where m is the vaporized liquid mass on the superficial layer, u the velocity of the expelled vapour
 143 mass, ρ the liquid density, R_0 the initial droplet radius and U the droplet propulsion velocity.

144 The primary parameter that determines the laser-induced droplet fragmentation, by establishing the
 145 propulsion velocity and thus, the expansion rate of the droplet, is the Weber number of the propelled
 146 droplet, defined as:

$$147 \quad We = \frac{\rho R_0 U^2}{\gamma} \quad (2)$$

148 where ρ is the liquid density, R_0 the initial droplet radius, U the droplet propulsion velocity and γ the
 149 liquid surface tension.

150 During the later-time droplet dynamics in Figure 1(iii-iv), the deformation of the droplet surface
 151 dominates on the inertial timescale, defined as $\tau_i = R_0/U$, until eventually the droplet lateral
 152 expansion is restricted by the surface tension and the extended fragmentation on the capillary
 153 timescale, calculated as $\tau_c = \sqrt{\rho R_0^3/\gamma}$.

154 **2.2. Early-time dynamics and initial fields**

155 The distinct separation of timescales in the laser-induced droplet fragmentation problem allows to
 156 isolate the modelling of the early-time droplet dynamics from the later-time droplet deformation and
 157 fragmentation without introducing physical or numerical restrictions. Following this observation,
 158 Gelderblom et al. [32] provided a unified analytical model for all early-time phenomena, starting from
 159 the laser-pulse impact onto the droplet for a duration τ_p , until the droplet propulsion with constant
 160 velocity on time τ_e , illustrated in Figure 1(i-ii). The model concerns a pressure pulse with magnitude p_e
 161 applied on the droplet surface for a duration τ_e . Accordingly, the absolute impulse scale $p_e \tau_e$ imposes
 162 the droplet propulsion. The momentum conservation at time τ_e is expressed, as follows:

$$163 \quad \int_0^{\tau_e} \int_A p_e e_z \cdot dA dt = \frac{4}{3} \pi \rho R_0^3 U \quad (3)$$

164 where τ_e is the vapour expulsion time, A the droplet surface area, p_e the magnitude of the pressure
 165 pulse, ρ the liquid density, R_0 the initial droplet radius, U the droplet propulsion velocity.

166 As derived from the assumptions of Gelderblom et al. [32] for an inviscid, irrotational and
 167 incompressible flow, the pressure field inside the droplet at time τ_e is obtained from the solution of
 168 the Laplace equation:

$$169 \quad \Delta p^* = 0 \quad (4)$$

170 for the non-dimensional pressure field $p^* = p/p_e$. Subsequently, the velocity field inside the droplet
 171 at time τ_e is calculated from the momentum equation, as:

$$172 \quad u = -\frac{\tau_e}{\rho} \nabla p \quad (5)$$

173 while the non-dimensional velocity field is obtained as $u^* = \rho R_0 u / p_e \tau_e$.

174 The pressure boundary condition of equation (4) refers to the original pressure pulse that is applied
175 on the droplet surface and considers the dependence of the pulse shape on the angle θ , such that:

$$176 \quad p^*(r = 1, \theta) = f(\theta) \quad (6)$$

177 where the pulse $f(\theta)$ is proportional to the actual laser pulse that impacts onto the droplet surface in
178 the conducted experiments of Klein et al. [23], [24], [25]. Therefore, Gelderblom et al. [32] suggested
179 a Gaussian-shaped pressure pulse to remain consistent with the typically used Gaussian laser-beam
180 profiles in the experiments. The Gaussian-shaped pressure pulse is formulated as:

$$181 \quad f(\theta) = c e^{-\frac{\theta^2}{2\sigma^2}} \quad (7)$$

182 where σ is the pulse width and $c = \frac{2\sqrt{2}}{\sigma \pi^{\frac{3}{2}} e^{-2\sigma^2} \left(2\operatorname{erfi}[\sqrt{2}\sigma] - \operatorname{erfi}\left[\frac{i\pi+2\sigma^2}{\sqrt{2}\sigma}\right] - \operatorname{erfi}\left[\frac{-i\pi+2\sigma^2}{\sqrt{2}\sigma}\right] \right)}$. In the experiments
183 of Klein et al. [23], a laser-beam profile with $\sigma = \pi/6$ is used; then, $c = 0.825$.

184 In the present numerical study, the previously presented analytical model for the early-time droplet
185 dynamics is adapted so as to be incorporated in the CFD framework. Specifically, the MEK droplet is
186 simulated as a 5° spherical wedge with one cell thickness in the azimuthal direction, using
187 pimpleFoam, a transient incompressible solver in OpenFOAM®. As suggested in the analytical model,
188 for times $t \leq \tau_e$, a pressure pulse is applied on the surface of the initially stagnant MEK droplet at
189 ambient conditions. Correspondingly, the pressure pulse is set as the pressure boundary condition on
190 the spherical wedge domain, given in dimensional form as:

$$191 \quad p(\theta) = p_e f(\theta) + p_{atm} \quad (8)$$

192 Details of the numerical configuration for the simulation of the early-time droplet dynamics are
193 illustrated in Figure 2(i).

194 At time $t = \tau_e$, the established pressure and velocity fields inside the droplet are calculated from the
195 numerical simulations, as illustrated qualitatively in Figure 2(ii). Later, the obtained flow fields are
196 utilized for the initialization of the droplet in the conducted numerical simulations that initiate at time
197 $t > \tau_e$ and capture the later-time phenomena, as demonstrated in §2.4.

198 **2.3. Later-time dynamics and numerical method**

199 The later-time phenomena, illustrated in Figure 1(iii-iv), are governed by the deformation of the
200 droplet into an elongated liquid sheet and the subsequent fragmentation of the droplet rim. The
201 detached fragments form a polydisperse cloud of secondary droplets with diameters at least two
202 orders of magnitude smaller than the initial droplet. Therefore, in the course of the phenomenon, a
203 flow field with dominant multiscale structures is developed, which imposes additional complexities in
204 a full-scale and computationally efficient numerical analysis.

205 In the present numerical study, the Σ - γ two-fluid model with dynamic local topology detection,
206 introduced in the previous work of the authors [34], is utilized for the laser-induced droplet rim
207 fragmentation simulations. The previously developed multiscale two-fluid approach provides a
208 physically consistent and numerically stable multiscale framework for the investigation of all the scales
209 involved in the laser-induced droplet fragmentation problem with a viable computational cost. A
210 fundamental principle of the multiscale framework is the detection of different flow regimes based
211 on advanced on-the-fly topological criteria and the application of the appropriate modelling approach
212 for the local interfaces based on the dimensions of the underlying structures. In particular, the

213 interface of the expanding but still coherent liquid sheet is fully resolved using the VOF sharp interface
 214 method [35], [36]. On the contrary, the produced fragments, which are smaller than the local mesh
 215 resolution, are modelled within a diffuse interface approach. In this case, an additional transport
 216 equation for the interface surface area density Σ [37], [38] is incorporated to model the unresolved
 217 sub-grid scale phenomena and provides an estimation for the dimensions of the unresolved sub-grid
 218 scale droplets.

219 The multiscale two-fluid approach has been implemented in OpenFOAM® with further developments
 220 on the twoPhaseEulerFoam solver in order to introduce all the additional features of the multiscale
 221 framework, as described in detail in [34]. The numerical model consists of the same set of governing
 222 equations under both formulations, namely the sharp and the diffuse interface approach, with specific
 223 source terms to be activated and deactivated depending on the currently operating formulation of the
 224 solver, as summarized below.

225 *Two-fluid model governing equations*

226 The volume averaged conservation equations [39] governing the balance of mass, momentum and
 227 energy for each continuum and inter-penetrating fluid phase k are:

$$228 \quad \frac{\partial}{\partial t}(a_k \rho_k) + \nabla \cdot (a_k \rho_k u_k) = 0 \quad (9)$$

$$229 \quad \frac{\partial}{\partial t}(a_k \rho_k u_k) + \nabla \cdot (a_k \rho_k u_k u_k) = -a_k \nabla p + \nabla \cdot (a_k \tau_k^{eff}) + a_k \rho_k g + \sum_{n=1}^2 M_{kn} \quad (10)$$

$$230 \quad \frac{\partial}{\partial t}[a_k \rho_k (e_k + k_k)] + \nabla \cdot [a_k \rho_k (e_k + k_k) u_k] = -\nabla \cdot (a_k \mathbf{q}_k^{eff}) - \left[\frac{\partial a_k}{\partial t} p + \nabla \cdot (a_k u_k p) \right] + a_k \rho_k g \cdot u_k + \sum_{n=1}^2 E_{kn} \quad (11)$$

231 where α_k is the volume fraction, ρ_k the density, u_k the velocity, e_k the specific internal energy, k_k the
 232 specific kinetic energy fields for each phase, p is the pressure field shared by both the liquid and
 233 gaseous phases and g the acceleration of gravity. Viscous and turbulence effects are introduced with
 234 the effective stress tensor τ_k^{eff} , which accounts for the molecular viscosity and the Reynolds stress
 235 tensor based on Boussinesq's hypothesis [40] and the effective heat flux vector \mathbf{q}_k^{eff} , which
 236 corresponds to the laminar and turbulent thermal diffusivity. M_{kn} represents the forces acting on the
 237 dispersed phase, depending on local topology; the surface tension force [41] is implemented under
 238 the sharp interface approach, while the aerodynamic drag force [42] is implemented under the diffuse
 239 interface approach. E_{kn} demonstrates the heat transfer between the liquid and gaseous phases,
 240 irrespectively of the flow region.

241 *Σ -Y model transport equations*

242 The transport equation for the liquid volume fraction in a compressible two-phase flow is given by:

$$243 \quad \frac{\partial a_l}{\partial t} + \nabla \cdot (a_l u_m) + v_{topo} [\nabla \cdot (a_l (1 - a_l) u_c)] = a_l a_g \left(\frac{\psi_g}{\rho_g} - \frac{\psi_l}{\rho_l} \right) \frac{Dp}{Dt} + a_l \nabla \cdot u_m - (1 - v_{topo}) R_{a_l} \quad (12)$$

244 where u_m is the velocity field of the liquid and gaseous mixture and ψ_l , ψ_g are the liquid and gaseous
 245 compressibility fields, respectively. v_{topo} distinguishes the two different interface approaches by taking
 246 either the 0 or 1 value under a diffuse or sharp interface formulation, respectively. Interface sharpness
 247 is imposed by the artificial compression velocity u_c . Additional modifications in the governing
 248 equations for coupling the VOF method with the two-fluid framework are presented in detail in [34].
 249 Finally, the term R_{a_l} accounts for the liquid dispersion induced by turbulent velocity fluctuations, which
 250 are important in dispersed flows and smaller scales [43], [44].

251 The transport equation for the liquid gas interface surface area density Σ [38] is given by:

$$252 \quad \frac{\partial \Sigma'}{\partial t} + \nabla(\Sigma' u_m) = (1 - v_{topo}) \left[-R_\Sigma + C_{SGS} \frac{\Sigma}{\tau_{SGS}} \left(1 - \frac{\Sigma}{\Sigma_{SGS}^*} \right) \right] \quad (13)$$

253 where the simultaneous existence of liquid and gas on the interface implies the presence of a
 254 minimum interface surface area density, such as $\Sigma = \Sigma' + \Sigma_{\min}$, as shown by Chesnel et al. [45]. The
 255 term R_Σ represents the interface surface area diffusion due to turbulent velocity fluctuations [44]. The
 256 sub-grid scale source term, namely the term $S_{SGS} = C_{SGS} \frac{\Sigma}{\tau_{SGS}} \left(1 - \frac{\Sigma}{\Sigma_{SGS}^*} \right)$, accounts for all the
 257 unresolved physical mechanisms which are responsible for the local interface formation. The S_{SGS} term
 258 is a function of the constant adjustable parameter C_{SGS} , the characteristic timescale τ_{SGS} and the
 259 critical interface surface area density Σ_{SGS}^* at an equilibrium state between interface production and
 260 destruction. Each modelled sub-grid scale mechanism has either a positive or a negative contribution
 261 on the overall S_{SGS} term calculation. Specifically, a positive S_{SGS} term value corresponds to an increase
 262 of the local interface surface area and physically correlates with the evolution of the underlying sub-
 263 grid scale droplets into smaller diameters, while a negative S_{SGS} term value describes a decrease of the
 264 local interface surface area due to the creation of sub-grid scale droplets with larger diameters.

265 In the present simulations of the laser-induced droplet fragmentation, the sub-grid scale modelling is
 266 implemented for the small-scale fragments detached from the droplet rim with sizes below the local
 267 mesh resolution. The evolution of the droplet sizes inside the produced cloud of fragments depends
 268 on the aerodynamic conditions of the surrounding air and on the sub-grid scale droplet interactions
 269 within the cloud. Therefore, the sub-grid scale mechanisms that are considered for the local interface
 270 formation are the effects of turbulence, the sub-grid scale droplet collision and coalescence, and the
 271 secondary breakup. The appropriate closure relations for each mechanism are based on models that
 272 are validated in the literature for similar flow conditions; the implemented sub-grid scale models and
 273 their limitations are discussed in detail in [46].

274 The diameter of a sub-grid scale fragment d_Σ is calculated as the equivalent diameter of a spherical
 275 particle which has the same volume to surface area ratio as the examined computational cell,
 276 proposed by Chesnel et al. [45] as:

$$277 \quad d_\Sigma = \frac{6\alpha_l(1-\alpha_l)}{\Sigma} \quad (14)$$

278 where α_l represents the liquid volume fraction and Σ the total liquid gas interface surface area density,
 279 as calculated in equation (13).

280 *Flow topology detection algorithm*

281 The flow topology detection algorithm is implemented based on general and case-independent
 282 topological criteria that can be applicable in any flow field governed by multiscale structures, as
 283 described in detail in [34]. For the present simulations of the laser-induced droplet fragmentation, the
 284 algorithm identifies instantaneous topological changes in the region around the droplet rim, where all
 285 the smaller-scaled structures are observed as a result of the rim breakup. Based on the sizes of the
 286 produced fragments, the algorithm evaluates and applies the most appropriate numerical
 287 formulation, namely an interface capturing approach for the sufficiently large structures or a sub-grid
 288 scale modelling for the unresolved fragments.

289 **2.4. Later-time simulation initialization and set-up**

290 The numerical simulations of the later-time droplet deformation and fragmentation initiate at time
 291 $t > \tau_e$ with ambient atmospheric conditions, while the flow field inside the droplet is initialized based
 292 on the modelling of the early-time phenomena in §2.2. The computational domain consists of a 5°
 293 wedge geometry with one cell thickness in the azimuthal direction and a mesh with a resolution of
 294 200 cells per original droplet diameter around the area of interest is applied. Details of the initial
 295 configuration for the simulations of the later-time phenomena are illustrated in Figure 2(iii). Different
 296 Weber numbers in the range of 90 to 750 are examined with corresponding droplet propulsion
 297 velocities between 1.76 m/s and 5.09 m/s. The simulation results are compared with the experimental
 298 observations of Klein et al. [25] for the same Weber numbers.

299 Regarding the numerical simulation set-up, the spatial discretization is based on second-order
 300 accurate discretization schemes. Time stepping is performed adaptively during the simulation to
 301 respect the selected limit for the convective Courant–Friedrichs–Lewy (CFL) condition of 0.2. The
 302 thermodynamic closure of the system is achieved by implementing the stiffened gas equation of state,
 303 proposed by Ivings et al. [47], for the liquid phase and the ideal gas equation of the state for the
 304 gaseous phase. Concerning the turbulence modelling, an LES approximation is implemented with the
 305 one-equation SGS model of Lahey [48]. However, the utilized computational domain imposes
 306 limitations regarding the accurate capturing of the turbulent state, which corresponds to fully 3D-
 307 developed phenomena. The simulations are initialized without turbulence in the flow field, since the
 308 droplet acceleration at early-times involves low velocities and Reynolds numbers around 10^3 .
 309 Therefore, in the absence of developed turbulence at the initial conditions, the LES approximation can
 310 be applied in the present geometry of one cell thickness in the azimuthal direction without significant
 311 modelling restrictions.

312 A crucial parameter for an accurate simulation of the later-time droplet deformation and
 313 fragmentation is the initialization of the pressure and velocity fields inside the droplet at time $t = \tau_e$,
 314 as obtained from the early-time simulations of §2.2. For a given Weber number, the droplet propulsion
 315 velocity is obtained from equation (2) and subsequently, the absolute impulse scale $p_e \tau_e$ can be
 316 calculated from equation (3), as introduced by Gelderblom et al. [32]:

$$317 \quad p_e \tau_e = \frac{\rho R_0 U}{3} \quad (15)$$

318 As shown in equation (15), different combinations of recoil pressure p_e and vapour expulsion time τ_e
 319 values determine different initialization sets (p_e, τ_e) for the same propulsion velocity U . Two conditions
 320 should apply for a valid expulsion time τ_e obtained for a known propulsion velocity; first, $\tau_e \gg \tau_p$ so
 321 that compressibility effects inside the droplet will not be significant and thus, the modelling
 322 assumption of an incompressible flow will not be violated and second, $\tau_e \ll \tau_i$ so that the applied
 323 pressure pulse will not have a macroscopic influence on the droplet spherical shape and thus, the
 324 droplet will not deform yet.

325 In Appendix A, it is validated that similarly with the analytical solution of Gelderblom et al. [32], the
 326 droplet deformation obtained from the proposed later-time simulations is dependent only on the
 327 absolute impulse scale and not on the individual p_e, τ_e values selected for a given propulsion velocity.

328 **3. Results and discussion**

329 The laser-induced rim fragmentation for a MEK droplet at $We = 330$ is presented in Figures 3 and 4,
 330 comparing the simulation results with the experimental observations of Klein et al. [25]. Following the
 331 impact of the millijoule nanosecond laser pulse, the droplet has evolved into a thin liquid sheet
 332 surrounded by a cloud of fragments at time $0.056 \tau_c$ in Figure 3(i). Subsequently, the liquid sheet
 333 expands further in the lateral direction and at the same time, the observed rim breakup enhances the

334 fragments cloud with polydisperse droplets of various diameters. The expanding liquid sheet is
335 captured by the sharp interface formulation of the multiscale framework, while the detached
336 fragments are subject to the sub-grid scale modelling, as illustrated in Figure 3(ii). Within the cloud of
337 fragments, droplets with diameters between $0.09 \mu\text{m}$ and $9 \mu\text{m}$ are detected; the upper limit is
338 correlated with the smallest structures that can be resolved with the sharp interface method for a
339 local mesh resolution of 200 cells per initial diameter and the lower limit corresponds to the spatial
340 resolution of the utilized camera in the experiments. Overall, the numerically captured expanding
341 sheet follows the deforming shape and the curvature observed in the experiments, while the modelled
342 fragments are detected close to the liquid sheet during the early stages of fragmentation and move
343 further backwards at later times. Moreover, the radial dependence of the sheet thickness, which is
344 demonstrated in the experimental results in front view in Figure 4(i), is well predicted by the numerical
345 simulations. Specifically, the maximum thickness is found in the center of the liquid sheet and the
346 minimum thickness is observed close to the rim. In consistence with the experimental observations of
347 Klein et al. [25], the rim is captured as a slightly thicker border, as observed in the numerical results in
348 Figure 3(ii). At later times, a more uniform thickness is predicted along the expanding sheet length, as
349 displayed qualitatively in the liquid sheet isosurfaces in Figure 3(ii) and extracted from the indicative
350 calculations of the local thickness in Figure 4(ii). Additional simulations are conducted using the VOF
351 solver in OpenFOAM[®] with the same initialization of the problem. The VOF method results, presented
352 in Figures 3(iii) and 4(iii), show a good agreement with the respective results obtained with the
353 multiscale two-fluid approach, regarding the capturing of the liquid sheet deformation; nevertheless,
354 the VOF method excludes the sub-grid scale information for the produced fragments.

355 Focusing on the predictions of the multiscale two-fluid approach in Figures 3 and 4, at time $0.056 \tau_c$,
356 which corresponds to the inertial time τ_i with dominant droplet deformation, the numerical results
357 meet the experimental observations and accurately predict the macroscopic liquid sheet expansion.
358 At the same time, a cloud of fragments, that recirculate behind the expanding sheet, is captured, with
359 the largest droplets observed close to the rim.

360 Later, at time $0.112 \tau_c$, the liquid sheet thickness is reduced to about 7% of the initial droplet diameter.
361 The numerical results satisfactorily follow the deforming shape of the thin liquid sheet and the lateral
362 expansion, while smaller fragments are captured downstream. However, an early sheet breakup is
363 observed close to the rim, where the local thickness of the liquid sheet is considerably reduced; a
364 sheet breakup is not noticed in the experimental results at that time. Due to the axisymmetric
365 geometry used in the numerical simulations the liquid sheet fragments detach in the form of
366 concentric rings that move outwards, as illustrated in the 3D reconstructed numerical results in
367 Figures 3(ii) and 4(ii). The multiscale two-fluid approach predicts a similar early sheet breakup even
368 with a finer mesh of a 250 cells per initial droplet diameter in Figure 4(ii). In the VOF method results
369 in Figure 4(iii), the early sheet breakup is still present but developed in a smaller extent. The more
370 pronounced early sheet breakup in the results of the multiscale model compared to the VOF results is
371 related to the modelling of slip velocity effects; the relative velocity between the very thin liquid sheet
372 and the surrounding air locally exceeds the value of 20 m/s around the rim, i.e., approximately 6 times
373 higher than the droplet propulsion velocity, and thus, enhances the local sheet breakup. Overall, the
374 early sheet breakup is a numerical limitation that originates from the utilized moderate mesh
375 resolution which is found to be insufficient to accurately capture the significantly reduced sheet
376 thickness around the rim at $0.112 \tau_c$. However, the implementation of a very fine uniform mesh will
377 violate the fundamental principles of the multiscale two-fluid approach for computationally efficient
378 simulations, i.e., the multiscale framework is based on a moderate uniform mesh resolution that
379 accurately captures the large-scale structures and a sub-grid scale modelling for the unresolved small-
380 scale structures. Alternatively, the proposed multiscale framework should be extended to couple an

381 adaptive mesh refinement (AMR) algorithm with the sharp interface formulation. The AMR algorithm
382 would be able to resolve flow structures in the segregated flow regime that require significantly high
383 resolution, such as the expanding liquid sheet, without an effect on the sub-grid scale modelling
384 formulation of the numerical model; this development is beyond the scope of our first numerical study
385 on the laser-induced droplet fragmentation problem.

386 Following, at time $0.227 \tau_c$, the aforementioned numerical limitations are observed even more
387 pronounced due to the significantly reduced thickness of the expanding liquid sheet. The length of the
388 numerically captured coherent sheet is limited, while a trace of radial fragments follows the shape of
389 the coherent elongated sheet, which is shown in the experimental visualizations. The successive
390 detachment of radial fragments from the sheet rim is a numerical artefact, which is previously
391 recognized in the BI simulations of Gelderblom et al. [32] during advanced stages of the fragmentation
392 process. At the same time, the experimental results demonstrate the nucleation of holes on the liquid
393 sheet as the major fragmentation mechanism. As illustrated in Figure 4(i), the first holes are already
394 detected along the rim at $0.227 \tau_c$ and thus, the assumption for an axisymmetric flow field is disrupted.

395 Considering that the present study is the first attempt in the literature to provide numerical
396 simulations for the laser-induced droplet fragmentation, the comparison between the experimental
397 and numerical results in Figures 3 and 4 is introduced as an investigation of the numerical capabilities
398 of the proposed multiscale two-fluid approach. Overall, the observed numerical limitations, namely
399 the early sheet breakup and the loss of axisymmetry, arise only during advanced stages of the droplet
400 fragmentation process. Therefore, the numerical simulations presented later in this study focus on
401 the droplet deformation and rim fragmentation before the numerical limitations become significant.
402 Specifically, for the examined droplets and expansion rates, the numerical simulations are terminated
403 at a selected final time that corresponds to the development of a liquid sheet with thickness
404 approximately 10% of the initial droplet diameter on the central line; this is an acceptable limit before
405 the early breakup and the loss of axisymmetry dominate. The validity of the utilized mesh resolution
406 and geometry to accurately capture the underlying physical phenomena upon the laser-induced
407 droplet deformation and fragmentation until the selected final time is discussed in Appendix B.

408 The fast jetting, which is shown in the experimental results in Figure 3 to initiate from the center of
409 the deforming droplet, is a result of the laser-matter interaction, as previously discussed in Klein et
410 al. [25] and Reijers et al. [33]. The millijoule nanosecond laser pulse applied onto the droplet surface
411 results to strong shock waves and potential cavitation spots inside the droplet that can give rise to
412 bubbles collapse, interfacial instabilities and finally, a fast jetting moving forward with a velocity larger
413 than the propulsion velocity of the droplet. The absence of the fast jetting from the numerical results
414 is not a limitation of the proposed numerical method but a result of the implemented modelling for
415 the early-time droplet dynamics. Specifically, the present modelling approach of the early-time
416 dynamics does not account for the real laser pulse applied on the droplet for a duration τ_p . Instead, it
417 provides a unified modelling solution for both early-time dynamics phenomena, namely, the laser
418 pulse impact and the resulting droplet propulsion, using a pressure pulse p_e and a duration τ_e which
419 are introduced for modelling purposes and do not correspond to the real laser intensity and duration.
420 Alternatively, the fast jetting can be captured by avoiding the present modelling of the early-time
421 phenomena and applying the real laser pulse onto the droplet surface for the real impact duration τ_p .
422 In this case, a compressible numerical model with advanced high-order numerical schemes should be
423 implemented to capture the intense compressibility effects inside the droplet and thus, the
424 incompressibility assumption for the early-time droplet dynamics will be no longer valid. However,
425 considering the very small liquid mass injected, the investigation of the fast-jetting phenomenon
426 remains beyond the scope of this study.

427 The effect of the Weber number on the MEK droplet deformation and fragmentation is examined in
428 Figures 5-8 for Weber number values of 90, 170, 330, and 750 and the same width deformations,
429 corresponding to a liquid sheet with thickness 50%, 20% and 10% of the initial droplet diameter. Since
430 the Weber number reflects the droplet expansion rate, which is set by the droplet propulsion, the
431 examined width deformations are observed at very different times for each case. Already at the initial
432 conditions, the strong impact of the Weber number is pronounced, resulting to significantly increased
433 initial pressure and velocity magnitudes at higher Weber numbers. Specifically, for $We = 90$ in Figure
434 5, the initial pressure and velocity fields inside the droplet, as calculated from the early-time
435 simulations in order to reach a propulsion velocity of 1.76 m/s, have a maximum value of 4.4 bar and
436 10 m/s, respectively. On the contrary, at $We = 750$ in Figure 8, the stronger pressure pulse, applied on
437 the droplet during the early-time simulations for a propulsion velocity of 5.09 m/s, imposes initial
438 pressure and velocity fields with the same profile but significantly increased maximum values up to
439 50.1 bar and 31 m/s, respectively.

440 Focusing on the early times of the droplet deformation at $We = 750$, due to the strong initial pressure
441 kick, the formation of a low-pressure region inside the droplet is observed, which is related to the
442 creation of cavitation bubbles. As highlighted in Figure 8 at $0.01 \tau_c$, the developed low-pressure region
443 is significantly small compared to the total mass of the deforming droplet and thus, it does not affect
444 the macroscopic droplet expansion. Therefore, a cavitation model has not been implemented in the
445 multiscale framework for the examined conditions. Instead, a very small volume fraction of air of the
446 order of 10^{-6} , which corresponds to a typical nucleation volume fraction [49], is introduced in the
447 initial droplet volume fraction. Under this assumption, the small gaseous volumes inside the droplet
448 will expand after the significant pressure drop, causing expansion similar to those that would occur
449 with cavitation. Subsequently, when the low-pressure region reaches the backside of the propelled
450 droplet interface, the gaseous volumes collapse. Due to the minor breakup on the local interface, very
451 few nanoscale droplets are captured by the numerical model at $0.035 \tau_c$; these droplets do not
452 significantly influence the total fragments' population.

453 In the course of the laser-induced droplet deformation, the atmospheric pressure inside the droplet
454 is rapidly recovered in a few microseconds and a pressure distribution close to atmospheric conditions
455 is stabilized, before significant deformation is observed. Therefore, the droplet expansion is primarily
456 governed by the radial component of the velocity $u_{sheet}(y)$, which shows maximum values on the
457 expanding rim. More specifically, at early stages, until a liquid sheet with thickness $0.5d_0$ is developed
458 in Figures 5-8, the droplet deformation is the major phenomenon, while only a few droplets are
459 detached from the rim. During these times, $u_{sheet}(y)$ induces the dominant liquid sheet radial expansion
460 with the maximum values on the rim to be approximately two times higher than the droplet
461 propulsion velocity in each examined case. At later stages, when the liquid sheet thickness is reduced
462 further than 50%, the rim fragmentation becomes significant and hence, the droplet radial expansion
463 is restricted. As a result, $u_{sheet}(y)$ gradually decreases over time; indicatively, $u_{sheet}(y)$ maximum values
464 on the rim are decreased by approximately 17% and 11% between a liquid sheet with thickness $0.5d_0$
465 and $0.2d_0$ at $We = 90$ and $We = 750$, respectively. At the final time, when a liquid sheet with thickness
466 $0.1d_0$ is formed, the fragmentation rate is reduced and less fragments are detached, as observed more
467 evidently at lower Weber numbers in Figures 5 and 6. Accordingly, the moderate fragmentation
468 observed does not have a significant effect on the thin liquid sheet radial expansion and $u_{sheet}(y)$
469 maximum values on the rim remain almost unchanged compared to earlier times.

470 Overall, the numerical results in Figures 5-8 demonstrate that an increasing Weber number imposes
471 a faster deformation of the initial spherical droplet into an elongated liquid sheet and an earlier
472 breakup of the rim. Additionally, the effect of the Weber number on the shape of the deforming liquid

473 sheet concerning both the lateral expansion and the radial distribution of the thickness is highlighted.
474 Specifically, during the early stages of deformation, the droplet shows an almost identical shape in the
475 four examined cases for the same thickness reduction by 50%; the examined deformation is observed
476 at different times for each case in accordance with the Weber number dependent expansion rates.
477 However, at later times, when already a thin liquid sheet is formed, a higher Weber number leads to
478 an increased lateral expansion and thus, a more uniform thickness distribution for the same width
479 deformation on the central line. Indicatively, for a liquid sheet with thickness $0.2d_0$, the lateral sheet
480 expansion is increased by approximately 7% at $We = 330$ and by 13% at $We = 750$, compared to the
481 predicted expansion at $We = 90$ for the same thickness.

482 Alongside the liquid sheet lateral expansion, the rim fragmentation becomes significant over time, as
483 observed in Figures 5-8. For a liquid sheet with thickness $0.5d_0$ the first micro-scaled fragments are
484 detached from the rim, while at later times, when the liquid sheet thickness is reduced to $0.2d_0$, the
485 dominance of the rim fragmentation is pronounced with an extended cloud of fragments to be
486 developed in each examined Weber number case. On average, the largest fragments with diameters
487 above $1 \mu\text{m}$ are detected close to the rim and the smallest scales are observed at the edges of the
488 polydisperse cloud. On the contrary, at the final time, the fragmentation process is weakened. Then,
489 a significantly limited cloud of fragments is observed at lower Weber numbers in Figures 5 and 6, while
490 at higher Weber numbers in Figures 7 and 8, the cloud of fragments remains extended but on average
491 less and smaller-scaled fragments below $3 \mu\text{m}$ are detached. During the evolution of the rim
492 fragmentation, the newly formed fragments are detached from the rim with radial velocities
493 $u_{\text{fragments}}(y)$, comparable with the radial velocity of the rim $u_{\text{sheet}}(y)$ at the time of breakup, as also
494 observed in the experimental study of Klein et al. [25]. Afterwards, the fragments are subject to a
495 recirculation behind the liquid sheet, driven by the moving vortex that is created as a result of the
496 interaction between the propelled and expanding liquid sheet and the surrounding air. For a liquid
497 sheet with thickness $0.2d_0$, the developed flow vorticity is found to be intense in all cases illustrated
498 in Figure 5-8, with local air velocity values more than two times higher than the fragments' velocities.
499 During later stages, the flow vorticity is becoming less significant; however, it still influences the
500 increasing cloud of fragments at higher Weber numbers, as shown at $0.089 \tau_c$ and $0.062 \tau_c$ in Figures
501 7 and 8, respectively.

502 A quantitative comparison between the experimental observations of Klein et al. [25], the analytical
503 model of Villermaux & Bossa [50] and the simulation results using the VOF method and the multiscale
504 two-fluid approach is presented in Figure 9, examining the droplet radial expansion under the Weber
505 numbers examined before. In the numerical simulations, the droplet expansion is considered, until a
506 thin liquid sheet with maximum thickness 10% of the initial droplet diameter is formed. On the whole,
507 the numerical results capture the strong dependence of the droplet expansion rate on the Weber
508 number and satisfactorily follow the experimental observations. A better agreement between the
509 numerical and the experimental results is obtained at the later stages of the droplet expansion
510 process, as similarly observed for the analytical solution. However, in contrast with the analytical
511 model [50], the conducted numerical simulations can accurately capture all stages of the droplet
512 deformation from a flattened back side to an elongated liquid sheet; thus, the small deviation between
513 the numerical and experimental results at early times is not a limitation of the numerical model.
514 Similarly, in the study of Gelderblom et al. [32], the BI simulation results of a water droplet radial
515 expansion slightly deviate from the experimental observations especially at early times. Considering
516 that the BI simulations use the same early-time initialization of the laser-induced droplet
517 fragmentation problem as the present numerical study, the small delay of the droplet radial expansion
518 at early times can be related to the early-time simulations and the lack of the impulsive effect of the
519 laser-matter interaction in the modelling of early-time dynamics. With respect to the capability of the

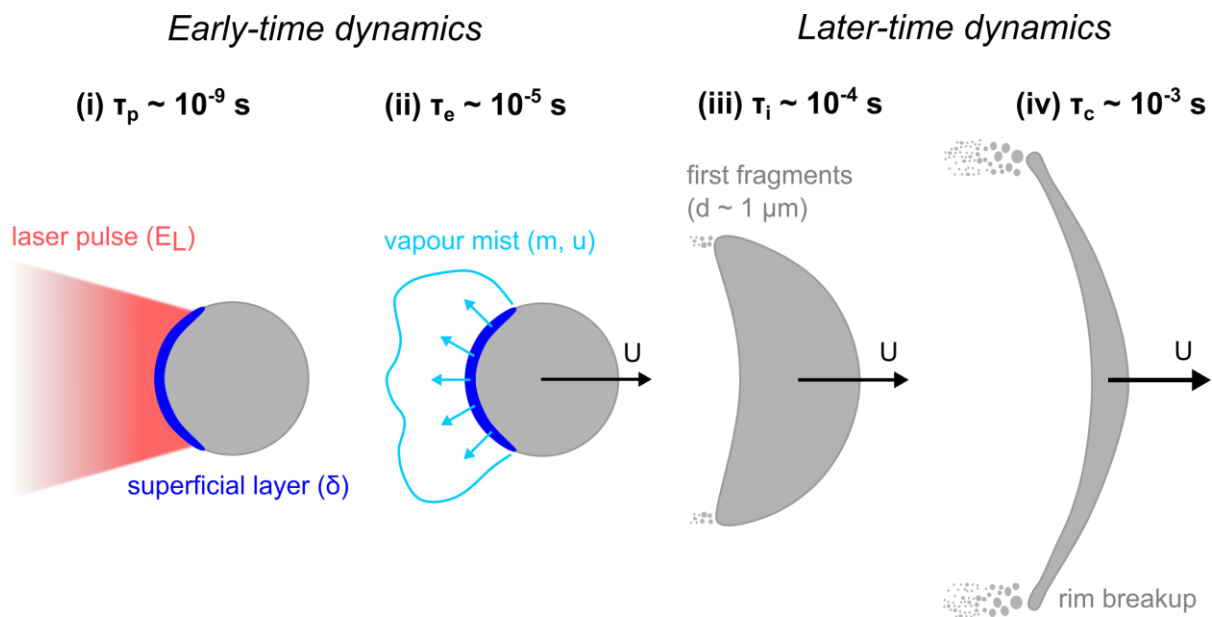
520 numerical methods to accurately capture the overall droplet deformation and radial expansion over
521 time, the VOF method results precisely follow the predictions of both the analytical model and the
522 experiments during the advanced stages of droplet expansion, while the multiscale two-fluid approach
523 results capture the phenomenon with on average a small delay of maximum 5% compared to the
524 calculations with the VOF method. The slightly delayed expansion, observed with the two different
525 numerical methods, can be related to the sub-grid scale modelling, which is performed within the
526 multiscale two-fluid approach and accounts for the produced fragments due to the rim breakup.
527 Under the multiscale framework, a part of the deformation energy that would be utilized for the
528 droplet radial expansion is now employed for the development of fragments. However, as depicted in
529 Figure 10, the volume concentration of the modelled fragments over the total volume of the liquid
530 phase increases significantly at higher Weber numbers. Thus, the production of fragments is not
531 negligible in the course of the droplet expansion and the resulting rim fragmentation. At lower Weber
532 numbers, the concentration of fragments relatively stabilizes during the rim fragmentation evolution,
533 while with an increasing Weber number, the fragments population is continuously enhanced over time
534 and even exceeds 40% of the total liquid volume at the later stages of rim fragmentation for the
535 highest examined Weber number of 750.

536 An overview of the evolution of the produced fragments inside the polydisperse cloud is depicted in
537 Figure 11, where the volume concentration of three classes of fragments with diameters $d_z > 1 \mu\text{m}$,
538 $0.5 \mu\text{m} < d_z < 1 \mu\text{m}$ and $0.09 \mu\text{m} < d_z < 0.5 \mu\text{m}$ is presented for a MEK droplet at $We = 90, 170, 330,$
539 750 over the total volume of the dispersed region. Upon the initiation of the laser-induced droplet rim
540 fragmentation, only large-scaled fragments of the first class above $1 \mu\text{m}$ are detected for each
541 examined Weber number case; these correspond to the first detached fragments from the rim.
542 Subsequently, more fragments are detached from the rim that enhance the fragments population,
543 while at the same time, the previously formed fragments interact with each other and develop further
544 inside the polydisperse cloud. The modelled sub-grid scale fragment interactions, namely the flow
545 turbulence, the droplet collision and coalescence and the secondary breakup effects, are driven by
546 the developed flow vorticity. Specifically, the moving vortex, which is forming behind the expanding
547 liquid sheet, enhances the local mixing and the slip effects between the newly formed micro-scaled
548 fragments of the first class and the surrounding air and leads to further breakup of the fragments
549 inside the cloud. On average, fragments of the second and third class with diameters below $1 \mu\text{m}$ are
550 not directly detached from the rim and are created at a second stage due to the droplet interactions
551 inside the cloud.

552 During later stages, when a liquid sheet with thickness $0.2d_0$ is formed, the rim fragmentation process
553 is fully developed, and an extended cloud of fragments is created downstream, as previously
554 illustrated in Figures 5-8. Then, the effect of the Weber number on the rim fragmentation rate and
555 the produced fragments population is pronounced. Specifically, for a liquid sheet with thickness $0.2d_0$
556 at $We = 90$ in Figure 11(i), the population of large-scaled fragments of the first class is significantly
557 decreased which can be related to the stabilization of the fragmentation mechanism and the reduction
558 of newly formed fragments, as shown in Figure 10. Instead, smaller-scaled fragments become
559 dominant, since the existing fragments inside the cloud are subject to further breakup driven by the
560 intense flow vorticity. On the contrary, for a liquid sheet with thickness $0.2d_0$ and higher Weber
561 numbers in Figures 11(ii-iv), the first class of fragments remains dominant, following the positive
562 fragmentation rate and the continuous enhancement of the dispersed cloud with newly formed
563 fragments, as depicted in Figure 10. At the same time, smaller scales become significant as a result of
564 the fragments interactions within the recirculating cloud; at $We = 170$ the third class of fragments is
565 more noticeable, while at $We = 330$ and $We = 750$ the population of fragments below $1 \mu\text{m}$ is more
566 balanced. Therefore, as observed for the examined cases, with increasing Weber number, the

567 intensity of the rim fragmentation mechanism is also increased and dominates over the fragments'
 568 interactions and breakup imposed by the developed flow vorticity.

569 During advanced stages of the rim fragmentation process for a liquid sheet with thickness around
 570 $0.1d_0$, the fragmentation rate weakens over time, even at higher Weber number cases of values 330
 571 and 750, as depicted in Figure 10. This is reflected in a less violent rim fragmentation and the creation
 572 of less and smaller newly formed fragments, as previously discussed in Figures 5-8. Consequently,
 573 smaller-scaled fragments below $1\ \mu\text{m}$ gradually dominate the fragments population and become even
 574 more significant at lower Weber numbers. Eventually, at the final time of the examined rim
 575 fragmentation, the predominant presence of the small-scaled fragments of the second and third class,
 576 i.e., fragments below $1\ \mu\text{m}$, is highlighted in the probability density functions (PDF) of the fragment
 577 sizes in Figure 12. The fragments sizes follow an exponential decrease in all Weber number cases, as
 578 indicatively plotted against the PDFs in Figure 12, with the largest captured fragments to be
 579 approximately $3\ \mu\text{m}$. At lower Weber numbers in Figures 12(i) and 12(ii), nearly 80% of the total
 580 fragments population consists of fragments below $1\ \mu\text{m}$; the pronounced dominance of small-scaled
 581 fragments comes in agreement with the previous observations of a limited number of newly formed
 582 fragments, as depicted in the stabilized volume concentration of the dispersed cloud in Figure 10. On
 583 the contrary, at higher Weber numbers in Figures 12(iii) and 12(iv), fragments below $1\ \mu\text{m}$ remain
 584 dominant in the population by 60%; however, the significant presence of larger-scaled fragments
 585 indicates that despite the attenuation of the fragmentation mechanism, the rim breakup continues to
 586 play a major role. Finally, a mesh convergence investigation for the calculated fragment populations
 587 is presented in Appendix C.



588

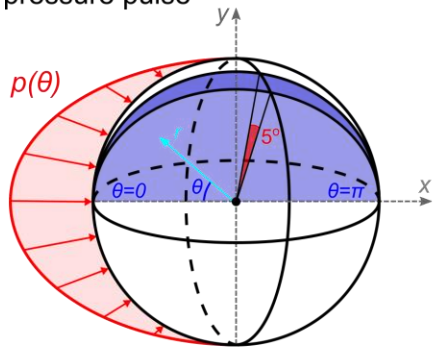
589 **Figure 1** Separation of timescales in the laser-induced droplet rim fragmentation problem. (i) A nanosecond laser pulse
 590 impacts onto the left side of the dyed droplet. (ii) The vaporized liquid mass on the superficial layer is ejected backwards. As
 591 a result, the droplet accelerates until it reaches a constant propulsion velocity U on the vapour expulsion time τ_e . (iii) The
 592 droplet propels and deforms on the inertial time τ_i . (iv) The surface tension and the extended fragmentation restrict the
 593 droplet lateral expansion on the capillary time τ_c .

Early-time dynamics

Later-time dynamics

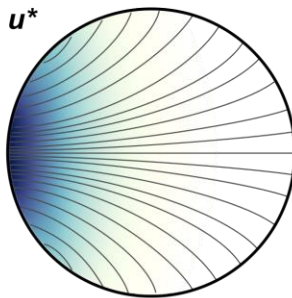
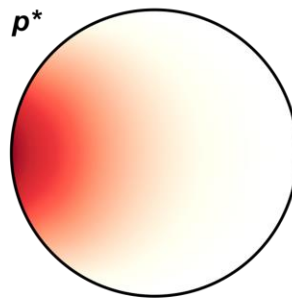
(i) $t < \tau_e$

pressure pulse



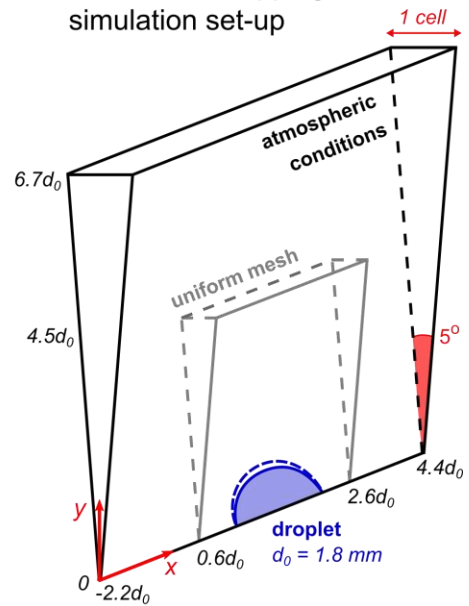
(ii) $t = \tau_e$

initial fields



(iii) $t > \tau_e$

initial fields mapping/
simulation set-up



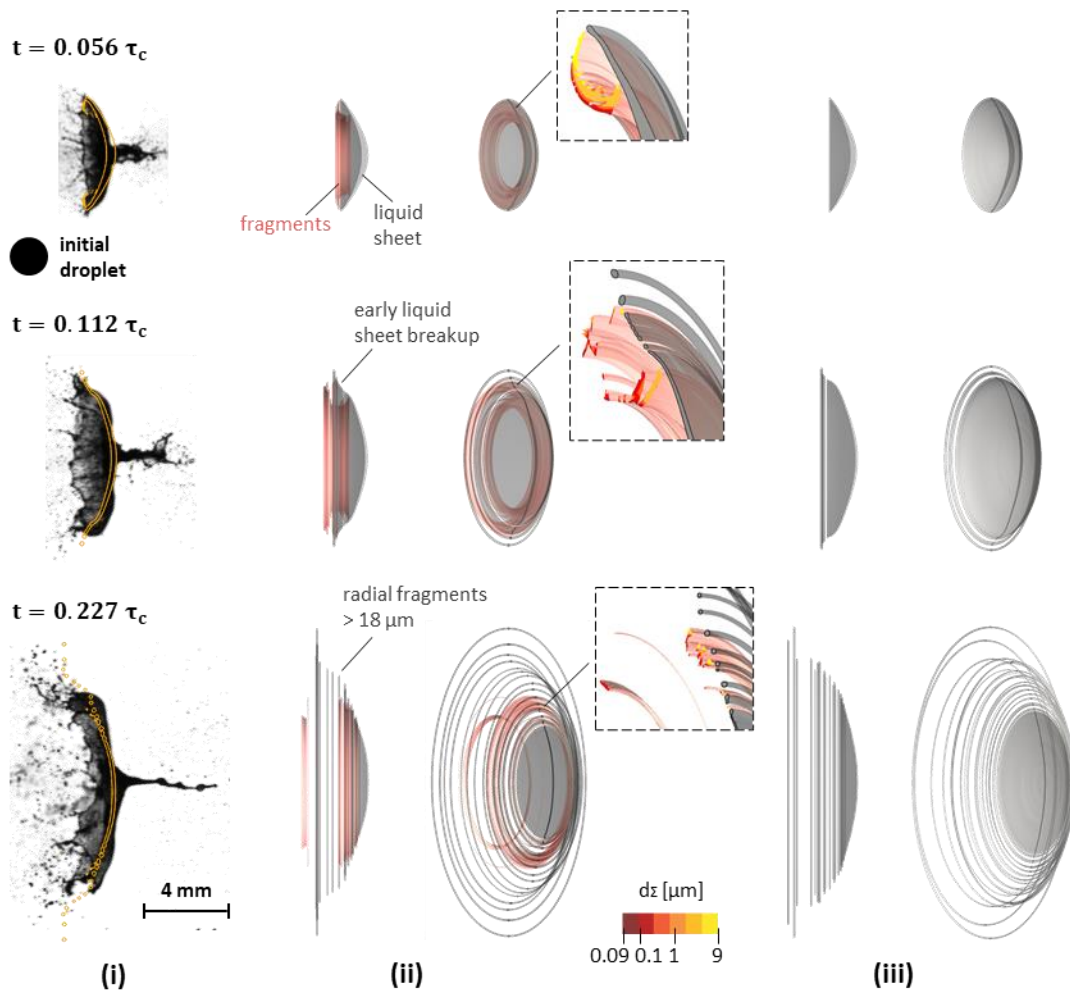
594

595

596

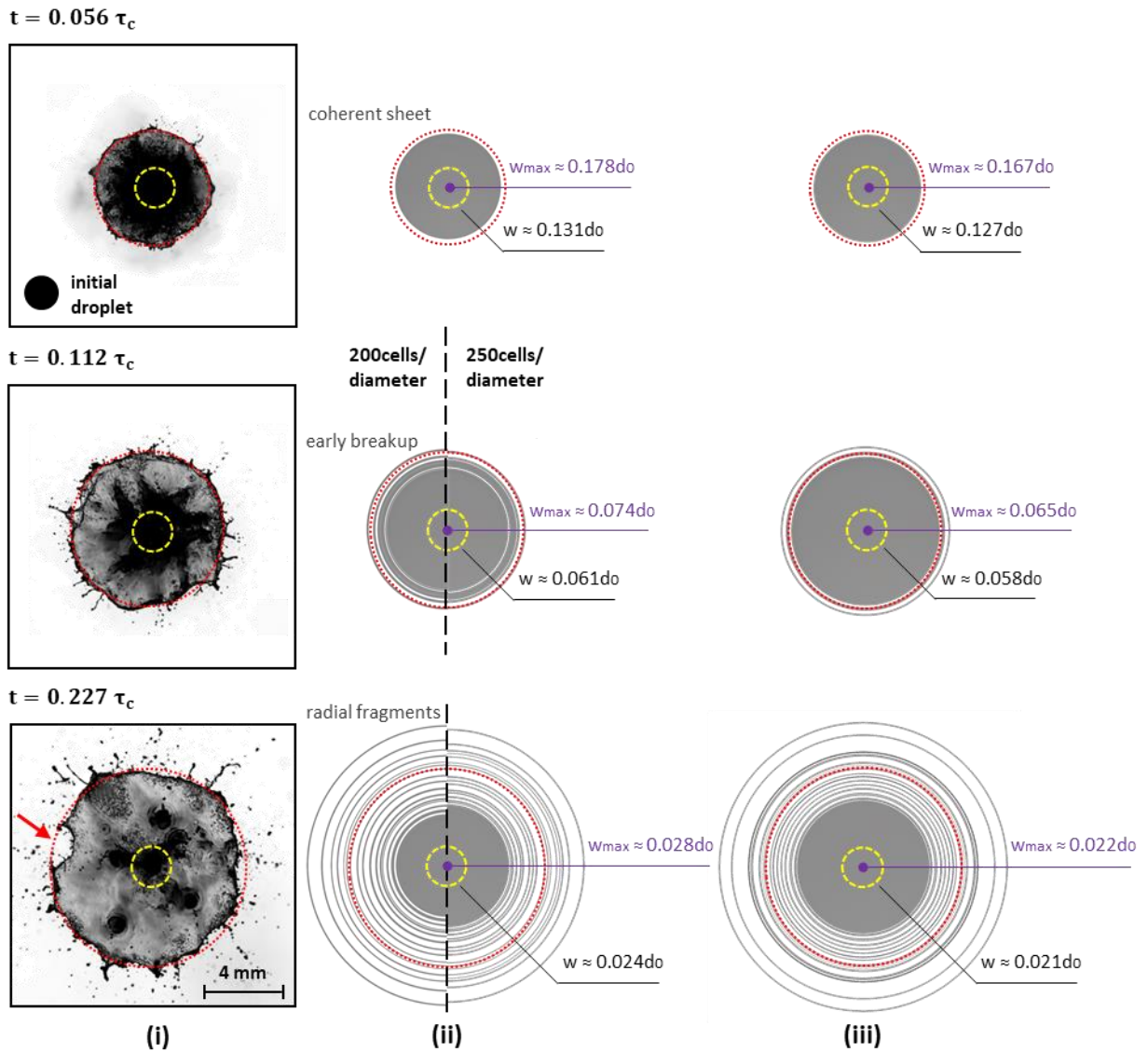
597

Figure 2 Problem configuration and simulation set-up. (i) For $t < \tau_e$, the axisymmetric pressure pulse $p(\theta)$ is applied on the droplet surface. (ii) At $t = \tau_e$, the initial pressure and velocity fields inside the droplet are obtained. (iii) The initial fields are mapped into the wedge geometry. For $t > \tau_e$, the droplet fragmentation is simulated using the multiscale two-fluid approach.



598

599 **Figure 3** Laser-induced droplet rim fragmentation at $We = 330$. (i) Comparison between the experimental visualizations of
 600 Klein et al. [25] in sideview and the isoline of the liquid volume fraction at 10^{-3} , obtained with the multiscale two-fluid
 601 approach. (ii) 3D reconstructed results in sideview and 30° angle, using the multiscale two-fluid approach. The expanding
 602 liquid sheet is captured by the sharp interface formulation (in grey the isosurface for liquid volume fraction at 0.5) and the
 603 detached fragments are captured by the diffuse interface formulation (in red the isosurface for fragments larger than
 604 $0.09 \mu\text{m}$). Zoomed-in view for the dimensions of the produced fragments after the rim breakup. (iii) 3D reconstructed results
 605 in sideview and 30° angle, using the VOF method. Isosurface of the liquid volume fraction at 0.5.

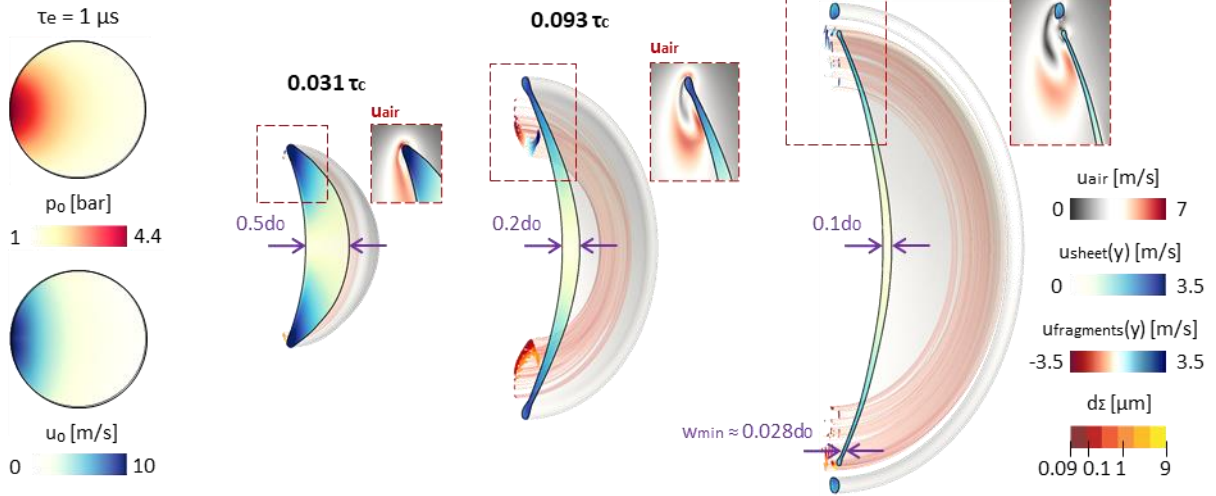


606

607
 608
 609
 610
 611
 612
 613

Figure 4 Laser-induced droplet rim fragmentation at $We = 330$. (i) Experimental visualizations of Klein et al. [25] in front view. (ii) 3D reconstructed results in front view, using the multiscale two-fluid approach. The expanding liquid sheet, captured by the sharp interface formulation, is illustrated as the isosurface of the liquid volume fraction at 0.5 with a mesh resolution of 200 (left) and 250 (right) cells per initial droplet diameter. (iii) 3D reconstructed results in front view, using the VOF method. Isosurface of the liquid volume fraction at 0.5 with a mesh resolution of 200 cells per initial droplet diameter. The red circle defines the borders of the liquid sheet rim in the experimental results. The calculated thickness of the thin liquid sheet on the central line (in purple) and on the initial droplet radius (in yellow) is illustrated on the simulation results.

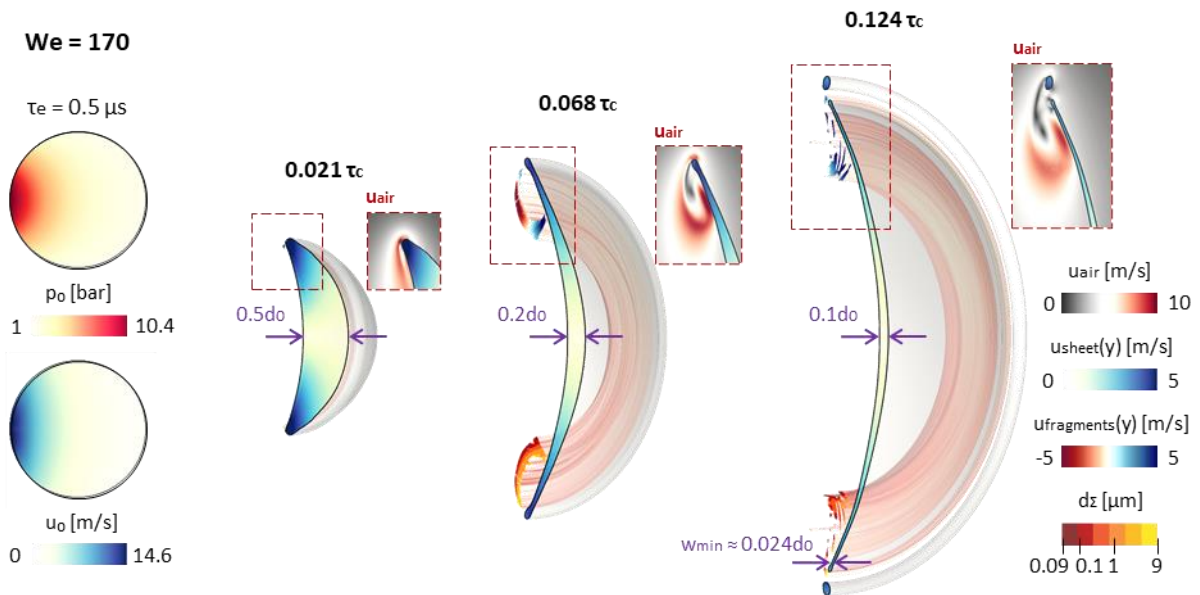
We = 90



614

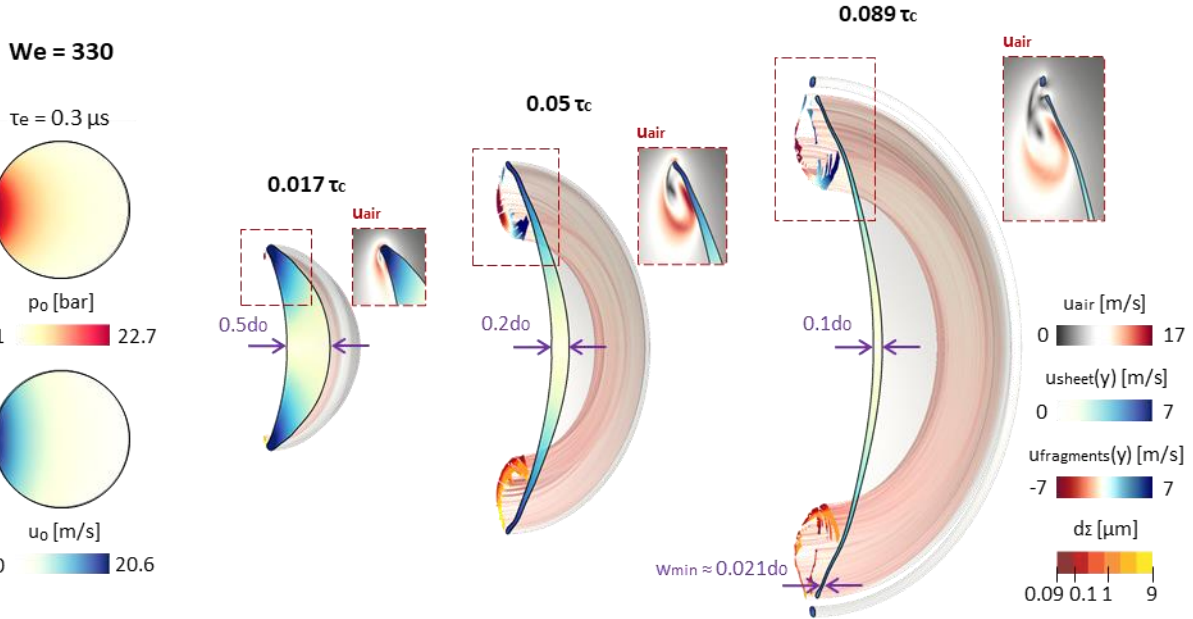
615 **Figure 5** Laser-induced droplet rim fragmentation at $We = 90$. Initial pressure and velocity fields inside the droplet, obtained
 616 for propulsion velocity $U = 1.76\text{m/s}$ and vapour expulsion time $\tau_e = 1 \mu\text{s}$. Liquid sheet expansion velocity in the lateral
 617 direction, radial velocity (top) and dimensions (bottom) of the detached fragments for three time-instances that correspond
 618 to a liquid sheet with thickness 50%, 20% and 10% of the initial droplet diameter. The air velocity field around the rim and
 619 the developed vortex are depicted on the side panels. The minimum captured thickness is illustrated at time $0.172 \tau_c$.

We = 170



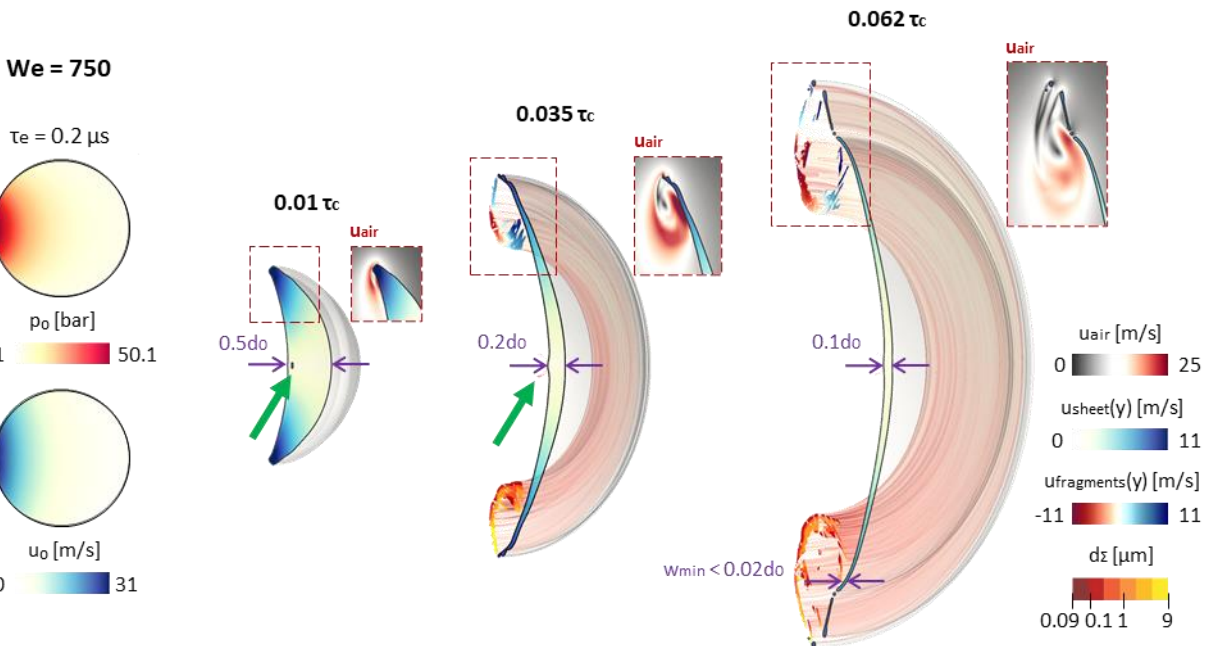
620

621 **Figure 6** Laser-induced droplet rim fragmentation at $We = 170$. Initial pressure and velocity fields inside the droplet, obtained
 622 for propulsion velocity $U = 2.42 \text{ m/s}$ and vapour expulsion time $\tau_e = 0.5 \mu\text{s}$. Liquid sheet expansion velocity in the lateral
 623 direction, radial velocity (top) and dimensions (bottom) of the detached fragments The air velocity field around the rim and
 624 the developed vortex are depicted on the side panels. The minimum captured thickness is illustrated at time $0.124 \tau_c$.



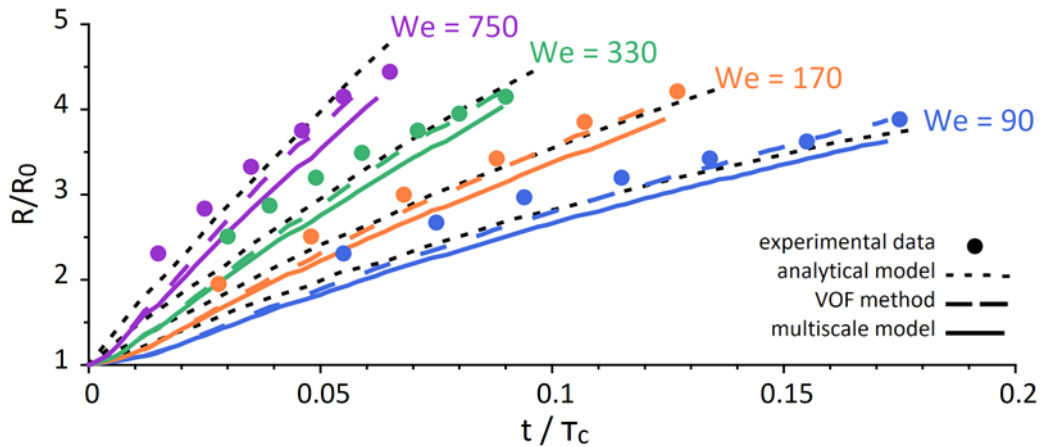
626

627 **Figure 7** Laser-induced droplet rim fragmentation at $We = 330$. Initial pressure and velocity fields inside the droplet, obtained
 628 for propulsion velocity $U = 3.37\text{m/s}$ and vapour expulsion time $\tau_e = 0.3 \mu\text{s}$. Liquid sheet expansion velocity in the lateral
 629 direction, radial velocity (top) and dimensions (bottom) of the detached fragments for three time-instances that correspond
 630 to a liquid sheet with thickness 50%, 20% and 10% of the initial droplet diameter. The air velocity field around the rim and
 631 the developed vortex are depicted on the side panels. The minimum captured thickness is illustrated at time $0.089 \tau_c$.



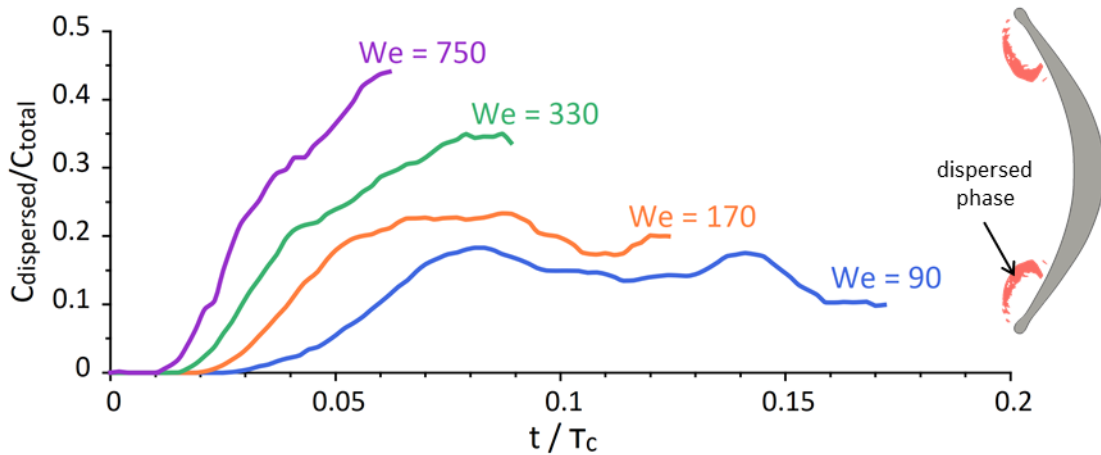
632

633 **Figure 8** Laser-induced droplet rim fragmentation at $We = 750$. Initial pressure and velocity fields inside the droplet, obtained
 634 for propulsion velocity $U = 5.09 \text{ m/s}$ and vapour expulsion time $\tau_e = 0.2 \mu\text{s}$. Liquid sheet expansion velocity in the lateral
 635 direction, radial velocity (top) and dimensions (bottom) of the detached fragments for three time-instances that correspond
 636 to a liquid sheet with thickness 50%, 20% and 10% of the initial droplet diameter. The air velocity field around the rim and
 637 the developed vortex are depicted on the side panels. The minimum captured thickness is illustrated at time $0.062 \tau_c$. The
 638 arrows point to the minor low-pressure region and the very few created droplets after collapse.



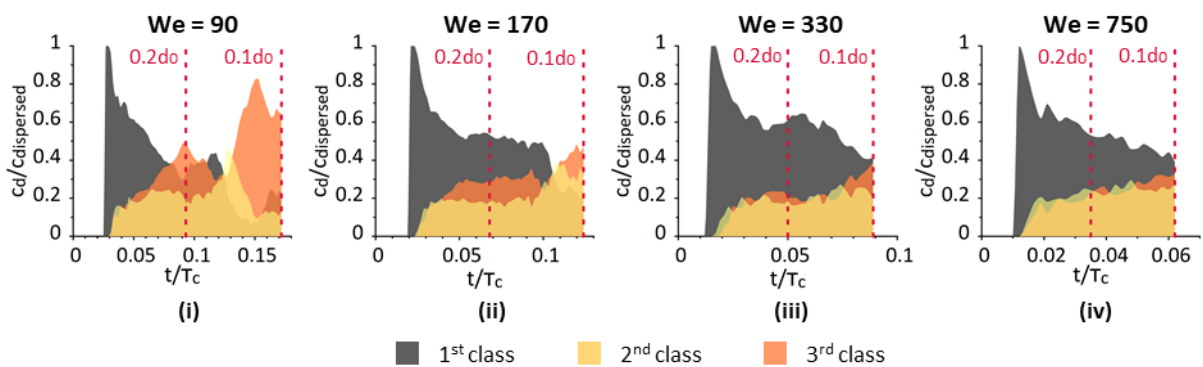
639

640 **Figure 9** Expansion of the liquid sheet radius, as a result of the laser-induced droplet deformation at $We = 90, 170, 330, 750$.
 641 Comparisons between the experimental observations of Klein et al. [25], the analytical model of Villermaux & Bossa [50] and
 642 the simulation results using the VOF method and the multiscale two-fluid approach until a liquid sheet with thickness 10%
 643 of the initial droplet diameter is formed.



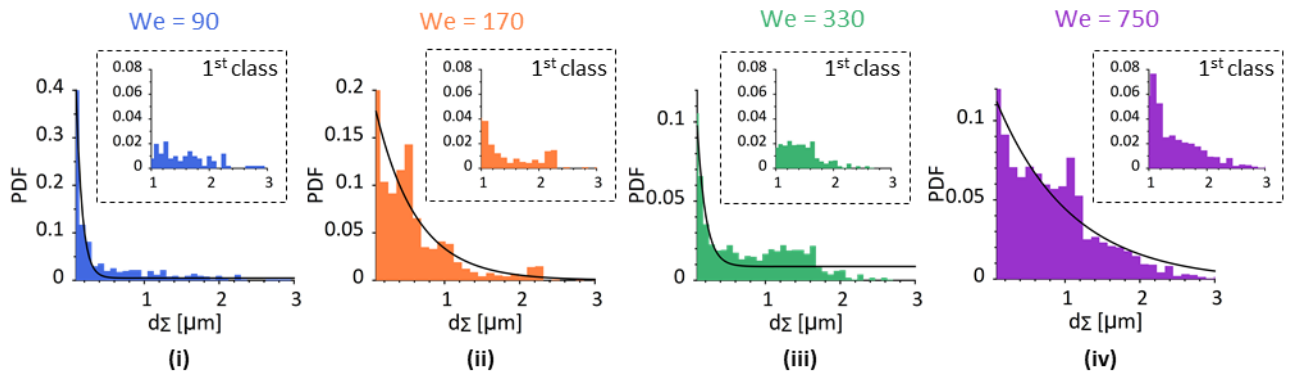
644

645 **Figure 10** Volume concentration of the dispersed region over the total volume of the liquid phase for the laser-induced
 646 droplet fragmentation at $We = 90, 170, 330, 750$.



647

648 **Figure 11** Volume concentration of three classes of fragments with diameters $d_z > 1 \mu\text{m}$ (1st class), $0.5 \mu\text{m} < d_z < 1 \mu\text{m}$ (2nd
 649 class) and $0.09 \mu\text{m} < d_z < 0.5 \mu\text{m}$ (3rd class) at $We = 90, 170, 330, 750$ over the total volume of the dispersed region. The
 650 vertical lines correspond to liquid sheet with thickness 20% and 10% of the initial droplet diameter.



651

652 **Figure 12** Probability density functions (PDF) of the fragment sizes at $We = 90, 170, 330, 750$ at the final time for a liquid
 653 sheet with thickness 10% of the initial droplet diameter. Zoomed-in view for the PDFs of the first class of fragments with
 654 diameters $d_{\Sigma} > 1 \mu\text{m}$. An exponential distribution is indicatively plotted against the PDF in each case.

655 **4. Conclusion**

656 The laser-induced droplet rim fragmentation for a millimetre-sized MEK droplet has been investigated
 657 in the present numerical study, examining a range of Weber numbers between 90 and 750 for the
 658 propelled droplet. The problem is characterized by the early-time droplet dynamics, imposed by the
 659 millijoule nanosecond laser-pulse impact and the subsequent response of the droplet until it reaches
 660 a constant propulsion velocity, and the later-time droplet dynamics, governed by the droplet
 661 deformation into an elongated liquid sheet and the resulting rim breakup. The early-time droplet
 662 dynamics were simulated within the CFD framework based on the analytical model of Gelderblom et
 663 al. [32] and the developed flow fields inside the droplet were obtained. Subsequently, the later-time
 664 droplet dynamics were simulated using the multiscale two-fluid approach, which allowed for the
 665 consideration of all the scales involved with a viable computational cost. Specifically, the radial
 666 expansion of the developed liquid sheet was resolved by the local mesh resolution, using the VOF
 667 sharp interface method, while the produced fragments due to the rim breakup were modelled under
 668 the diffuse interface approach with consideration of the significant sub-grid scale phenomena inside
 669 the cloud of fragments. The simulation results showed a good agreement with the experimental
 670 observations of Klein et al. [25] with respect to the shape and the expansion of the elongated liquid
 671 sheet and the development of a polydisperse cloud of fragments, until a selected final time before the
 672 numerical limitations and the nucleation of holes on the liquid sheet surface become significant.

673 The numerical simulations demonstrated the influence of the laser beam energy on the initial flow
 674 fields inside the droplet and the subsequent droplet deformation and rim fragmentation; the present
 675 observations have a general interest for different droplets and conditions but the same droplet Weber
 676 number. Specifically, with increasing Weber numbers, a higher expansion rate, a more uniform liquid
 677 sheet thickness and a more extended cloud of fragments at the later stages of fragmentation was
 678 captured. Quantitative information for the radial velocity fields, which are responsible for the droplet
 679 expansion, were provided, showing maximum values on the rim. Additionally, during the liquid sheet
 680 expansion, the formation of a moving vortex behind the rim was identified, as a result of the
 681 interaction between the expanding liquid sheet and the surrounding air; thus, the vortical flow creates
 682 a recirculation region for the produced fragments. Finally, an overview of the evolution of the
 683 fragments' population, during the droplet rim fragmentation and the sizes distributions at the final
 684 time of the phenomenon were presented. Overall, larger-scale fragments were detached from the rim
 685 at the early stages of fragmentation, while smaller fragments below $1 \mu\text{m}$ dominated at the later
 686 stages, as a result of the further breakup of the secondary droplets inside the cloud and the

687 attenuation of the fragmentation mechanism over time. However, with increasing Weber number,
 688 droplets above $1\ \mu\text{m}$ remain significant even at the final times.

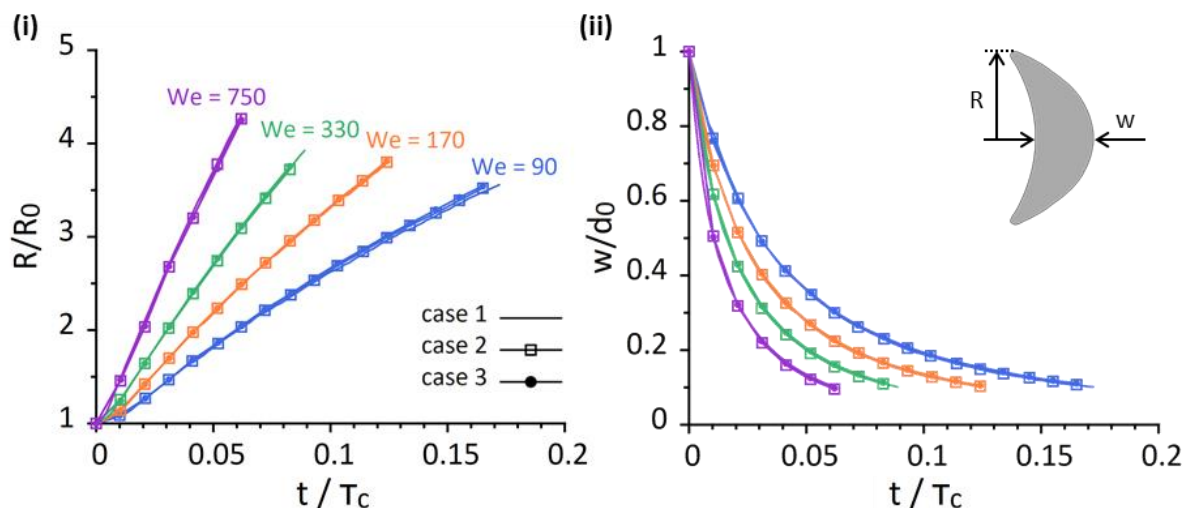
689 Further development of the proposed multiscale two-fluid approach to incorporate an AMR algorithm
 690 and phase-change phenomena, namely, a cavitation and vaporisation model, will provide a valuable
 691 numerical model to investigate a broader range of unsteady fragmentation problems and obtain an
 692 insight into the sizes of the produced fragments that is not easily accessible from the experimental
 693 observations. Examples of fragmentation cases of interest in the literature to date include the violent
 694 laser-induced droplet fragmentation in biofuels [51] and screen printing inks [52], the explosive
 695 droplet fragmentation [22] and the surface jet breakup [53] by laser-induced cavitation bubbles and
 696 the breakup of laser-induced jets in needle-free medical injections [54], among others.

697 Acknowledgements

698 This work was supported by the European Union Horizon-2020 Research and Innovation Programme
 699 (Haos Project), Grant Agreement No 675676. Additional funding has been received by the UK's
 700 Engineering and Physical Sciences Research Council (EPSRC) through grant EP/K020846/1. The authors
 701 gratefully acknowledge the valuable help and fruitful discussions with Dr. Pierre Chantelot and
 702 Professor Detlef Lohse about the physics of the laser-induced droplet deformation and fragmentation
 703 and the initialization of the performed simulations upon the early investigations of the present study.

704 Appendix A. Later-time simulations initialization and effect on droplet deformation rate

705 The absolute impulse scale $p_e\tau_e$ defines the later-time droplet dynamics and the resulting droplet
 706 deformation for a given propulsion velocity. However, as shown in equation (15), for a specified
 707 impulse scale $p_e\tau_e$, different initialization sets (p_e , τ_e) can be derived and equivalently used for the
 708 initialization of the later-time simulations at $t = \tau_e$. In Figure 13, the droplet radial expansion and
 709 width reduction is demonstrated for the examined MEK droplet at Weber numbers 90, 170, 330, and 750,
 710 using three different initialization sets for each Weber number. Overall, the droplet deformation rate
 711 remains almost unaffected by the different initialization sets of the same problem, similarly with the
 712 previous observations of Gelderblom et al. [32].



713

714 **Figure 13** Evolution of the laser-induced droplet deformation at $We = 90, 170, 330,$ and 750 . (i) Droplet radius expansion and
 715 (ii) droplet width reduction for three different initialization sets, namely same impulse scale $p_e\tau_e$ but different individual p_e ,
 716 τ_e values, for each examined propulsion velocity and until a liquid sheet with thickness 10% of the initial droplet diameter is
 717 formed.

718 **Appendix B. Validity of numerical model: mesh resolution and geometry**

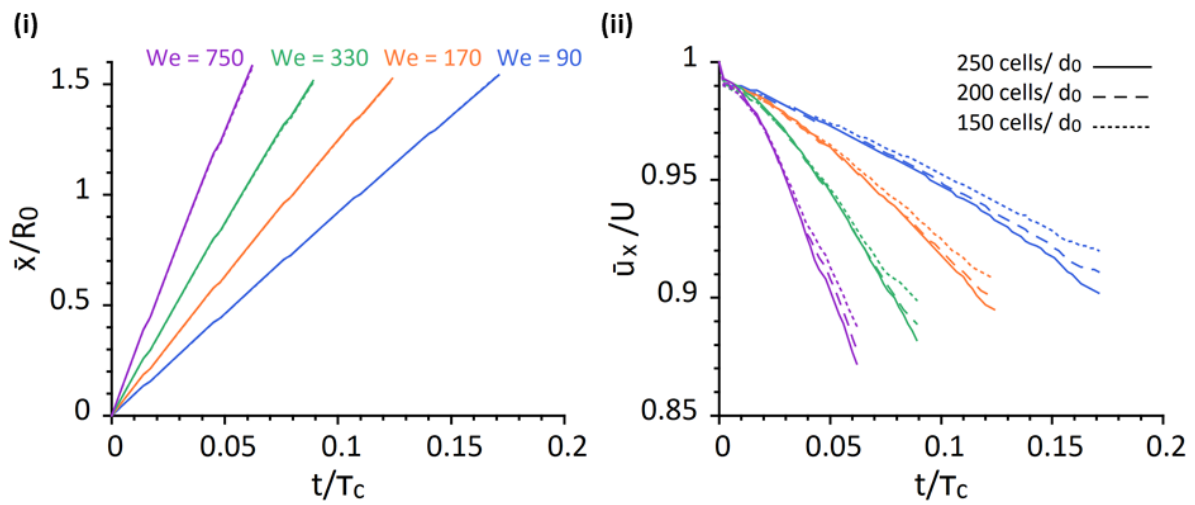
719 The capability of the proposed multiscale two-fluid approach to accurately capture the laser-induced
720 droplet deformation and rim fragmentation until the selected final time of the numerical simulations
721 is discussed below; the selected final time corresponds to the development of a liquid sheet with
722 thickness 10% of the initial droplet diameter on the central line. The investigation focuses on the two
723 major aspects that can raise limitations in the conducted simulations, namely the convergence of the
724 numerical solution and the accuracy of the axisymmetric assumption.

725 *1. Mesh convergence investigation*

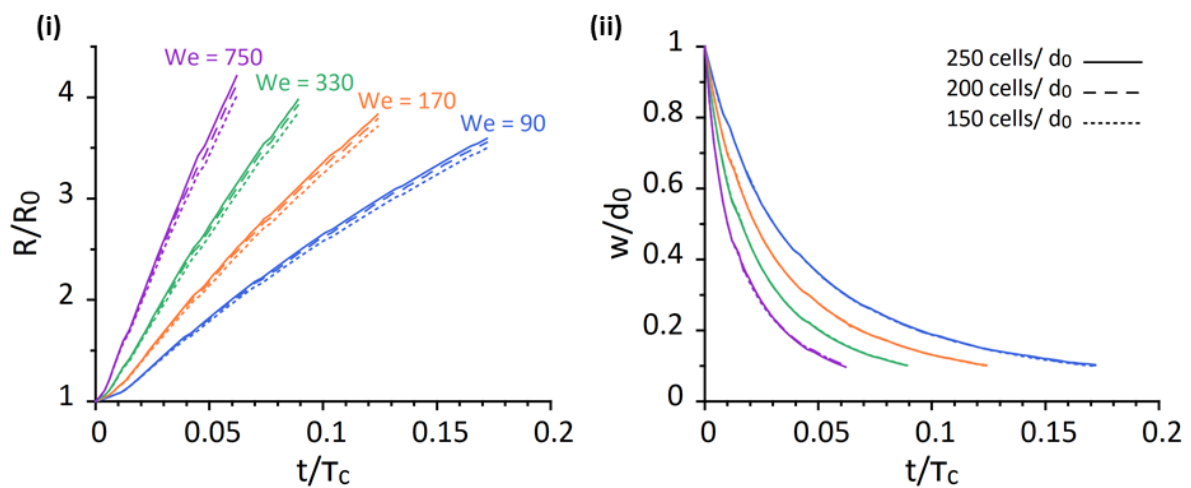
726 The droplet response to the laser pulse impact is related to three main macroscopic physical
727 phenomena, the droplet propulsion, deformation, and fragmentation. Each phenomenon is
728 investigated below with respect to the convergence of the numerical solution for a MEK droplet at We
729 = 90, 170, 330, and 750 using three different mesh resolution of 150, 200 and 250 cells per initial
730 droplet diameter until the selected final time of the numerical simulations.

- 731 • The center-of-mass properties in the axial direction in Figure 14 depict the droplet propulsion.
732 Both the axial position and the axial velocity of the center-of-mass are accurately captured by all
733 the applied mesh resolutions. The small decrease of the axial center-of-mass velocity over time
734 is observed more rapid with an increasing Weber number due to the effect of the surrounding air
735 that becomes more significant at higher propulsion velocities, i.e., the center-of-mass velocity is
736 reduced by approximately 10% and 13% at the final time for $We = 90$ and 750, respectively.
737
- 738 • The droplet radial and axial deformation is illustrated in Figure 15; the measurements of the
739 droplet radial expansion converge with an increasing mesh resolution, while a very good
740 agreement is demonstrated for the measurements of the droplet axial deformation irrespectively
741 of the utilized mesh.
742
- 743 • The evolution of the rim fragmentation is investigated in Figure 16, illustrating the volume
744 concentration of the dispersed phase over the total volume of the liquid phase for different
745 Weber numbers and mesh resolutions, as obtained within the Eulerian-Eulerian framework of
746 the multiscale two-fluid approach; namely, the fragments volume over time is calculated based
747 on the liquid volume fraction and not on the absolute volume of the detached fragments. As a
748 result, even though the absolute number of fragments is continuously increasing over time, very
749 dilute liquid regions within the cloud of fragments that correspond to significantly low liquid
750 volume fractions and equivalent fragment diameters below $0.09 \mu\text{m}$ are excluded. This
751 phenomenon is more pronounced at low Weber numbers 90 and 170; here, the fragmentation
752 rate attenuates at the later stages and significantly less large-scale fragments are detached from
753 the rim which is depicted as a non-monotonous concentration of fragments in Figure 16. Overall,
754 the concentration of dispersed fragments captured within the multiscale framework converges
755 towards the solution obtained with the finest mesh, concerning the initiation of the rim breakup
756 and the progressive detachment of fragments over time. Specifically, at Weber numbers 330 and
757 750, the intermediate mesh results with a resolution of 200 cells/ d_0 are found to approach more
758 closely the finest mesh solution during the later stages of fragmentation compared to the lower
759 Weber number cases with values 90 and 170. However, at lower Weber numbers, the rim
760 fragmentation is less violent, and the concentration of fragments relatively stabilizes over time.
761 As a result, the deviation between the results for a resolution of 200 and 250 cells/ d_0 is mainly
762 enhanced by new fragments below $1 \mu\text{m}$. Thus, it is safe to conclude that the calculated

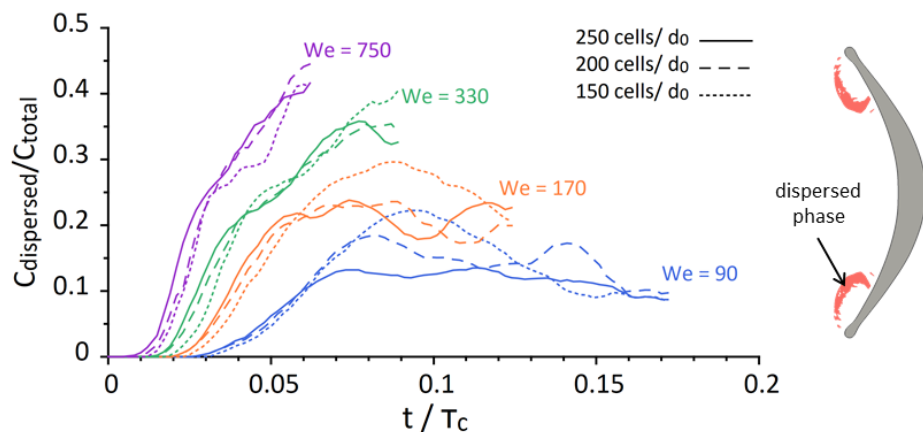
763 concentrations of fragments using the multiscale two-fluid approach satisfactorily converge in all
 764 examined conditions.



765
 766 **Figure 14** Centre-of-mass properties for a MEK droplet at $We = 90, 170, 330,$ and 750 . (i) Position and (ii) velocity of the
 767 centre-of-mass in the axial direction. Mesh convergence investigation using three different mesh resolutions of 150, 200 and
 768 250 cells per initial droplet diameter.



769
 770 **Figure 15** Evolution of the laser-induced deformation for a MEK droplet at $We = 90, 170, 330,$ and 750 . (i) Droplet radius
 771 expansion and (ii) droplet width reduction. Mesh convergence investigation using three different mesh resolutions of 150,
 772 200 and 250 cells per initial droplet diameter.



774 **Figure 16** Evolution of the laser-induced rim fragmentation for a MEK droplet at $We = 90, 170, 330,$ and 750 . Volume
775 concentration of the dispersed phase over the total volume of the liquid phase. Mesh convergence investigation using three
776 different mesh resolutions of 150, 200 and 250 cells per initial droplet diameter.

777 2. Axisymmetric modelling assumption

778 An axisymmetric geometry is commonly adopted in numerical simulations of droplet fragmentation
779 cases, as an acceptable compromise between a satisfactory representation of the developed physics
780 and a viable computational cost. Various examples of axisymmetric simulations using a $\sim 5^\circ$ wedge
781 geometry can be found in the literature, such as the explosive fragmentation imposed by a laser-
782 induced cavitation in the study of Zeng et al. [22] and the droplet fragmentation due to mechanical
783 impact onto a solid surface with moderate [55], [56] and high impact velocities [31], [34].

784 The laser-induced droplet fragmentation, examined here, is an unsteady fragmentation process,
785 characterized by two fragmentation modes, namely, the rim and the sheet fragmentation, as
786 identified by Klein et al. [25]. The present numerical study focuses on the investigation of the rim
787 fragmentation, simulated until a selected final time before the sheet fragmentation begins. During the
788 rim fragmentation, perturbations with a characteristic wave number form along the rim and evolve
789 into fragments, i.e., ligaments or droplets. The fastest-growing wave number upon the unsteady rim
790 fragmentation for liquids of small viscosity is introduced by Wang et al. [57], as follows:

$$791 \quad k_{max}^* = \sqrt{\frac{1}{2 + \frac{6\sqrt{2}}{Re}}} \quad (16)$$

792 where k_{max}^* is non-dimensionalized by the rim diameter b , such that $k_{max}^* = k_{max}/(b/2)$. \widetilde{Re} is the
793 local rim Reynolds number which is calculated, as follows:

$$794 \quad \widetilde{Re} = 0.20h^{-5/4}Re^{-1/4} \quad (17)$$

795 where $Oh = \mu/\sqrt{\rho\gamma d_0}$ and $Re = Ud_0/\nu$ are the Ohnesorge and Reynolds numbers, respectively, for
796 the properties of the initial droplet before fragmentation, i.e., d_0 is the initial droplet diameter, U the
797 propulsion velocity, μ the dynamic viscosity, ρ the density, γ the surface tension and ν the kinematic
798 viscosity.

799 For the examined MEK droplet at Weber numbers 90, 170, 330, and 750, the fastest-growing wave
800 number obtained from equation (16) is $k_{max} \cong 0.33b$ in dimensional form. Considering the 5° wedge
801 geometry used and the progressive radial expansion of the droplet, the critical point to examine if the
802 developed wave numbers fit in the utilized wedge geometry is during the initiation of the rim
803 fragmentation process. At this moment for each examined case, the droplet radius is expanded by
804 $R \cong 1.5R_0$, the azimuthal dimension of the wedge around the rim is $z_{min} \cong 10^{-4}m$ and the rim
805 diameter is $b \cong 10^{-4}m$. As a result, even during the initiation of the rim fragmentation process, the
806 fastest-growing wave number can fit in the 5° wedge geometry, since $k_{max} \cong 0.33 \times 10^{-4} < z_{min}$.
807 Overall, the axisymmetric 5° wedge geometry is an acceptable modelling compromise in the
808 conducted simulations without suppressing the developed wave numbers and thus, influencing the
809 results.

810 On the contrary, the simulation of the Rayleigh-Taylor instability-driven sheet fragmentation would
811 require not only a 3D geometry but also a significantly high resolution around the extremely thin liquid
812 sheet in order to accurately resolve the non-axisymmetric hole nucleation. In practice, this numerical
813 investigation would mean a computationally expensive Direct Numerical Simulation (DNS). However,
814 a computationally efficient simulation within the developed multiscale framework would be possible

815 with a further development of the proposed numerical model so as to couple an adaptive mesh
816 refinement (AMR) algorithm with the sharp interface formulation. Then, the AMR algorithm would
817 provide high resolution around the expanding but still coherent liquid sheet, sufficient to resolve the
818 resulting hole nucleation and at the same time, operate independently of the sub-grid scale modelling
819 for the produced micro-scale fragments. This new model development is beyond the scope of the
820 present study, our first numerical study on the laser-induced droplet fragmentation problem and is
821 part of the ongoing research.

822 **Appendix C. Droplet size distributions: mesh convergence investigation**

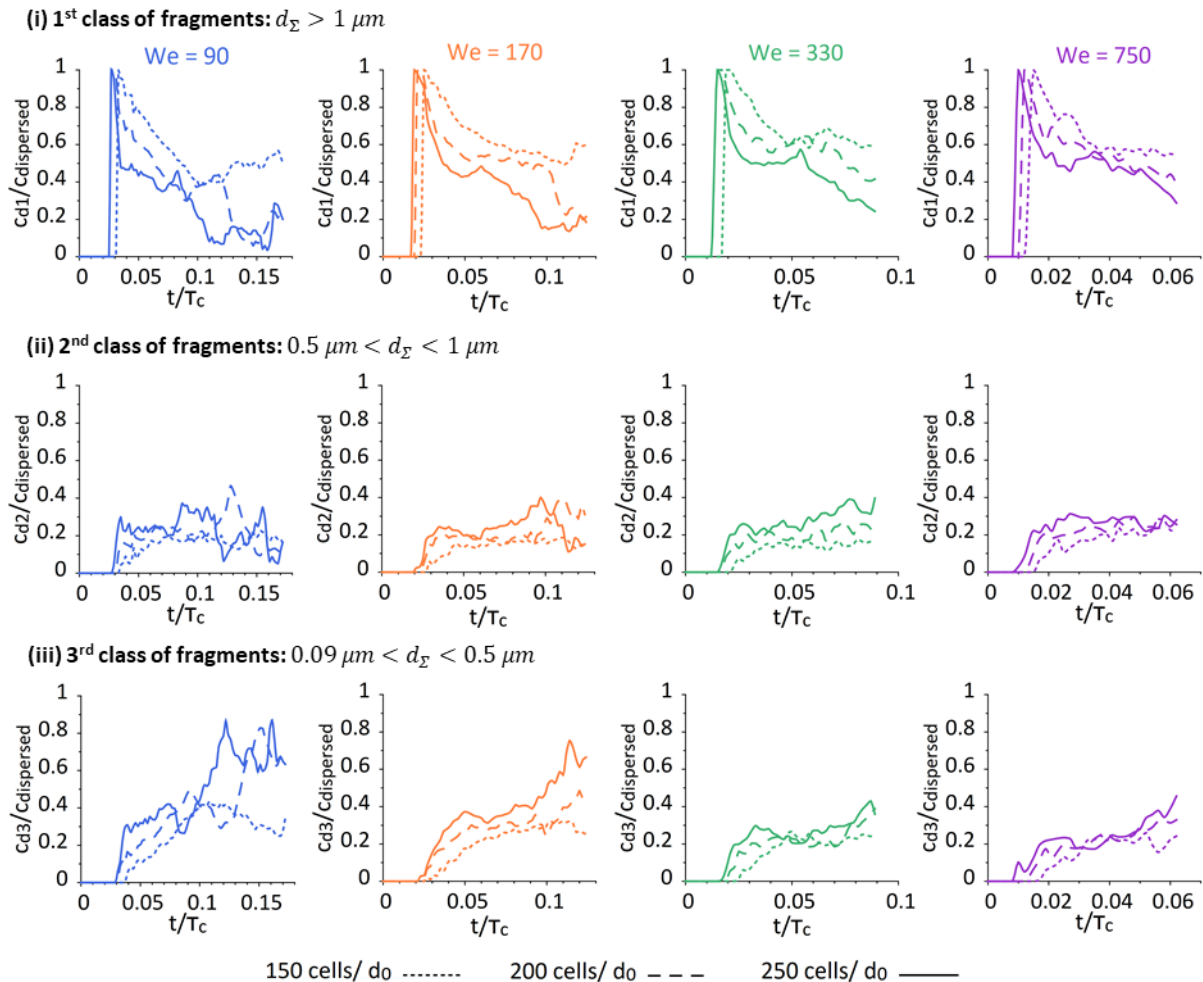
823 The diameter of a sub-grid scale fragment is calculated within the multiscale two-fluid approach in
824 equation (14) as the equivalent diameter of a spherical particle which has the same volume to surface
825 area ratio as the examined computational cell. Therefore, the fragment diameter is a function of the
826 local calculated interface surface area density and the computational cell volume. In practice, for the
827 same examined computational volume, a very coarse mesh will predict a single large droplet, while a
828 finer mesh will capture the same volume with multiple computational cells and thus, will predict a
829 group of smaller droplets, one in each cell. As a result, a coarser mesh enhances the calculation of
830 larger diameters, while in a finer mesh smaller diameters will dominate. Following this modelling
831 limitation, a moderate mesh resolution is the safest balance to obtain the most accurate
832 representation of the physics and restrict the mesh-related overestimation of larger or smaller
833 droplets.

834 Considering the inevitable modelling effect of the mesh resolution on the droplet size calculations, the
835 interest of a mesh convergence investigation does not lie in the individual diameter values at a specific
836 time. Instead, the overall evolution of the fragments' population over time, examining how specific
837 classes of diameters develop upon the rim fragmentation process, is here the most significant. In
838 Figure 17, the volume concentration of three classes of fragments, same as in Figure 11, with
839 diameters $d_z > 1 \mu\text{m}$, $0.5 \mu\text{m} < d_z < 1 \mu\text{m}$ and $0.09 \mu\text{m} < d_z < 0.5 \mu\text{m}$ is illustrated for a MEK droplet at
840 $We = 90, 170, 330,$ and 750 over the total volume of the dispersed region, using three different mesh
841 resolutions.

842 For the highest droplet propulsion velocities with corresponding Weber number values of 330 and
843 750, the concentration of droplets over time follows the same tendency in the three presented classes
844 of fragments in Figure 17, irrespectively of the mesh resolution used. As expected, the largest
845 fragments of the first class are found to be more significant with the coarsest mesh of 150 cells/ d_0
846 even during the later stages of rim fragmentation, while the smaller fragments of the second and third
847 class are more pronounced with the finest mesh of 250 cells/ d_0 . For $We = 330$, the droplet size
848 distribution of Figure 12 is obtained at the final time $0.089 \tau_c$, when the maximum observed deviation
849 between the moderate and the finest mesh results is found for the concentration of the first class of
850 fragments and is approximately 15%. For $We = 750$, the droplet size distribution of Figure 12 is
851 obtained at $0.062 \tau_c$ with the concentration of the first class of fragments to differ by less than 10%
852 between the mesh of 200 and 250 cells/ d_0 . Overall, the observed small deviations between the
853 calculated concentrations of different classes of fragments for Weber number values of 330 and 750
854 do not violate the overall capturing of the phenomenon.

855 Focusing on the lower propulsion velocities with Weber number values of 90 and 170 and the first
856 class of fragments in Figure 17(i), the concentration of the largest droplets class is reduced significantly
857 earlier with the finest mesh of 250 cells/ d_0 . As previously shown in Figure 16, after $0.06 \tau_c$, the overall
858 concentration of fragments relatively stabilizes; thus, at this time, the fragmentation process
859 decelerates, and less newly formed fragments are detached from the rim. As a result, the developed

860 cloud of fragments is not as varied as previously and mainly consists of droplets around 1 μm , instead
 861 of a group of large droplets well above 1 μm close to the rim that break down into smaller droplets
 862 downstream. In this case, the effect of the mesh resolution on the droplet size calculations around 1
 863 μm is pronounced; the mesh of 150 cells/ d_0 overestimates the first class of droplets, while the mesh
 864 of 250 cells/ d_0 underestimates their presence in the cloud of fragments. However, for the time
 865 instances that the droplet size distributions of Figure 12 are obtained, the moderate mesh resolution
 866 results satisfactorily converge towards the finest mesh solution; for $We = 90$, the maximum deviation
 867 is less than 4% for the second class of fragments, while for $We = 170$, the maximum deviation is
 868 observed for the third class of fragments and a difference of 18%.



869
 870 **Figure 17** Volume concentration of three classes of fragments for a MEK droplet at $We = 90, 170, 330,$ and 750 over the total
 871 volume of the dispersed region, using three different mesh resolutions of 150, 200 and 250 cells per initial droplet diameter.

872 References

- 873 [1] S. Fujioka, M. Shimomura, Y. Shimada, S. Maeda, H. Sakaguchi, Y. Nakai, T. Aota, H.
 874 Nishimura, N. Ozaki, A. Sunahara, K. Nishihara, N. Miyanaga, Y. Izawa, and K. Mima, *Pure-Tin*
 875 *Microdroplets Irradiated with Double Laser Pulses for Efficient and Minimum-Mass Extreme-*
 876 *Ultraviolet Light Source Production*, Appl. Phys. Lett. **92**, 241502 (2008).
- 877 [2] H. Mizoguchi, T. Abe, Y. Watanabe, T. Ishihara, T. Ohta, T. Hori, T. Yanagida, H. Nagano, T.
 878 Yabu, S. Nagai, G. Soumagne, A. Kurosu, K. M. Nowak, T. Sukanuma, M. Moriya, K. Kakizaki, A.
 879 Sumitani, H. Kameda, H. Nakarai, and J. Fujimoto, *100W 1st Generation Laser-Produced*
 880 *Plasma Light Source System for HVM EUV Lithography*, in *Extreme Ultraviolet (EUV)*

- 881 *Lithography II. International Society for Optics and Photonics*, Vol. 7969 (2011), p. 796908.
- 882 [3] V. Y. Banine, K. N. Koshelev, and G. H. P. M. Swinkels, *Physical Processes in EUV Sources for*
883 *Microlithography*, J. Phys. D. Appl. Phys. **44**, 253001 (2011).
- 884 [4] A. Pirati, J. van Schoot, K. Troost, R. van Ballegoij, P. Krabbendam, J. Stoeldraijer, E. Loopstra,
885 J. Benschop, J. Finders, H. Meiling, E. van Setten, N. Mika, J. Dredonx, U. Stamm, B. Kneer, B.
886 Thuring, W. Kaiser, T. Heil, and S. Migura, *The Future of EUV Lithography: Enabling Moore's*
887 *Law in the next Decade*, in *Extreme Ultraviolet (EUV) Lithography VIII*, Vol. 10143 (2017), p.
888 101430G.
- 889 [5] N. Bloembergen, *Brief History of Laser-Induced Breakdown*, in *Laser-Induced Damage in*
890 *Optical Materials: 1998*, Vol. 3578 (International Society for Optics and Photonics, 1999), pp.
891 198–200.
- 892 [6] E. M. Gattass, Rafael R., *Femtosecond Laser Micromachining in Transparent Materials*, Nat.
893 Photonics **2**, 219 (2008).
- 894 [7] G. Della Valle, R. Osellame, and P. Laporta, *Micromachining of Photonic Devices by*
895 *Femtosecond Laser Pulses*, J. Opt. A Pure Appl. Opt. **11**, (2009).
- 896 [8] M. M. Krasnov, *Laser-Phakopuncture in the Treatment of Soft Cataracts*, Br. J. Ophthalmol.
897 **59**, 96 (1975).
- 898 [9] J. T. Walsh, *Pulsed Laser Angioplasty: A Paradigm for Tissue Ablation*, in *Optical-Thermal*
899 *Response of Laser-Irradiated Tissue* (1995), pp. 865–902.
- 900 [10] A. Vogel and V. Venugopalan, *Mechanisms of Pulsed Laser Ablation of Biological Tissues*,
901 Chem. Rev. **103**, 577 (2003).
- 902 [11] I. Aplitz and A. Vogel, *Material Ejection in Nanosecond Er:YAG Laser Ablation of Water, Liver,*
903 *and Skin*, Appl. Phys. A Mater. Sci. Process. **81**, 329 (2005).
- 904 [12] S. R. G. Avila and C. D. Ohl, *Fragmentation of Acoustically Levitating Droplets by Laser-Induced*
905 *Cavitation Bubbles*, J. Fluid Mech. **805**, 551 (2016).
- 906 [13] M. S. Krivokorytov, Q. Zeng, B. V. Lakatos, A. Y. Vinokhodov, Y. Y. Sidelnikov, V. O.
907 Kompanets, V. M. Krivtsun, K. N. Koshelev, C. D. Ohl, and V. V. Medvedev, *Shaping and*
908 *Controlled Fragmentation of Liquid Metal Droplets through Cavitation*, Sci. Rep. **8**, 1 (2018).
- 909 [14] P. Kafalas and J. Herrmann, *Dynamics and Energetics of the Explosive Vaporization of Fog*
910 *Droplets by a 106-Mm Laser Pulse*, Appl. Opt. **12**, 772 (1973).
- 911 [15] P. Kafalas and A. P. Ferdinand, *Fog Droplet Vaporization and Fragmentation by a 106-Mm*
912 *Laser Pulse*, Appl. Opt. **12**, 29 (1973).
- 913 [16] V. Prasad Sandireddy, K. Prasad Koirala, G. Duscher, and R. Kalyanaraman, *Explosive*
914 *Vaporization of Metallic Nanostructures on a Surface by Nanosecond Laser Heating under*
915 *Fluids*, J. Appl. Phys. **129**, 064901 (2021).
- 916 [17] J.-Z. Zhang, J. K. Lam, C. F. Wood, B.-T. Chu, and R. K. Chang, *Explosive Vaporization of a Large*
917 *Transparent Droplet Irradiated by a High Intensity Laser*, Appl. Opt. **26**, 4731 (1987).
- 918 [18] D. Kurilovich, A. L. Klein, F. Torretti, A. Lassise, R. Hoekstra, W. Ubachs, H. Gelderblom, and O.
919 O. Versolato, *Plasma Propulsion of a Metallic Microdroplet and Its Deformation upon Laser*
920 *Impact*, Phys. Rev. Appl. **6**, (2016).
- 921 [19] R. G. Pinnick, A. Biswas, R. L. Armstrong, S. G. Jennings, J. D. Pendleton, and G. Fernández,
922 *Micron-Sized Droplets Irradiated with a Pulsed CO₂ Laser: Measurement of Explosion and*

- 923 *Breakdown Thresholds*, Appl. Opt. **29**, 918 (1990).
- 924 [20] M. M. Basko, M. S. Krivokorytov, A. Yu Vinokhodov, Y. V. Sidelnikov, V. M. Krivtsun, V. V.
925 Medvedev, D. A. Kim, V. O. Kompanets, A. A. Lash, and K. N. Koshelev, *Fragmentation*
926 *Dynamics of Liquid-Metal Droplets under Ultra-Short Laser Pulses*, Laser Phys. Lett. **14**, 36001
927 (2017).
- 928 [21] S. Y. Grigoryev, B. V. Lakatosh, M. S. Krivokorytov, V. V. Zhakhovsky, S. A. Dyachkov, D. K.
929 Ilnitsky, K. P. Migdal, N. A. Inogamov, A. Y. Vinokhodov, V. O. Kompanets, Y. V. Sidelnikov, V.
930 M. Krivtsun, K. N. Koshelev, and V. V. Medvedev, *Expansion and Fragmentation of a Liquid-*
931 *Metal Droplet by a Short Laser Pulse*, Phys. Rev. Appl. **10**, 064009 (2018).
- 932 [22] Q. Zeng, S. R. Gonzalez-Avila, S. Ten Voorde, and C.-D. Ohl, *Jetting of Viscous Droplets from*
933 *Cavitation-Induced Rayleigh–Taylor Instability*, J. Fluid Mech. **846**, 916 (2018).
- 934 [23] A. L. Klein, W. Bouwhuis, C. W. Visser, H. Lhuissier, C. Sun, J. H. Snoeijer, E. Villermaux, D.
935 Lohse, and H. Gelderblom, *Drop Shaping by Laser-Pulse Impact*, Phys. Rev. Appl. **3**, 1 (2015).
- 936 [24] A. L. Klein, D. Lohse, M. Versluis, and H. Gelderblom, *Apparatus to Control and Visualize the*
937 *Impact of a High-Energy Laser Pulse on a Liquid Target*, Rev. Sci. Instrum. **88**, (2017).
- 938 [25] A. L. Klein, D. Kurilovich, H. Lhuissier, O. O. Versolato, D. Lohse, E. Villermaux, and H.
939 Gelderblom, *Drop Fragmentation by Laser-Pulse Impact*, J. Fluid Mech. **893**, (2020).
- 940 [26] E. Villermaux, *Fragmentation*, Ann. Rev. Fluid Mech. **39**, 419 (2007).
- 941 [27] D. C. K. Rao, A. P. Singh, and S. Basu, *Laser Pulse-Droplet Interaction Enables the Deformation*
942 *and Fragmentation of Droplet Array*, (2021).
- 943 [28] P. Koukouvinis, N. Kyriazis, and M. Gavaises, *Smoothed Particle Hydrodynamics Simulation of*
944 *a Laser Pulse Impact onto a Liquid Metal Droplet*, PLoS One **13**, 1 (2018).
- 945 [29] D. R. Gueldenbecher, C. Lopez-Rivera, and P. E. Sojka, *Secondary Atomization*, Exp. Fluids **46**,
946 371 (2009).
- 947 [30] Z. Wu and Y. Cao, *Dynamics of Initial Drop Splashing on a Dry Smooth Surface*, PLoS One **12**, 1
948 (2017).
- 949 [31] G. Tretola and K. Vogiatzaki, *Numerical Treatment of the Interface in Two Phase Flows Using a*
950 *Compressible Framework in OpenFOAM: Demonstration on a High Velocity Droplet Impact*
951 *Case*, Fluids **6**, 78 (2021).
- 952 [32] H. Gelderblom, H. Lhuissier, A. L. Klein, W. Bouwhuis, D. Lohse, E. Villermaux, and J. H.
953 Snoeijer, *Drop Deformation by Laser-Pulse Impact*, J. Fluid Mech. **794**, 676 (2016).
- 954 [33] S. A. Reijers, J. H. Snoeijer, and H. Gelderblom, *Droplet Deformation by Short Laser-Induced*
955 *Pressure Pulses*, J. Fluid Mech. **828**, 374 (2017).
- 956 [34] G. Nykteri, P. Koukouvinis, R. S. Gonzalez Avila, C.-D. Ohl, and M. Gavaises, *A Σ -Y Two-Fluid*
957 *Model with Dynamic Local Topology Detection : Application to High-Speed Droplet Impact*, J.
958 Comput. Phys. **408**, 109225 (2020).
- 959 [35] C. W. Hirt and B. D. Nichols, *Volume of Fluid (VOF) Method for the Dynamics of Free*
960 *Boundaries*, J. Comput. Phys. **39**, 201 (1981).
- 961 [36] R. Scardovelli and S. Zaleski, *Direct Numerical Simulation of Free-Surface and Interfacial Flow*,
962 Annu. Rev. Fluid Mech. **31**, 567 (1999).
- 963 [37] A. Vallet and R. Borghi, *Modelisation Eulerienne de l'atomisation d'un Jet Liquide*, Comptes

- 964 Rendus l'Académie Des Sci. IIB-Mechanics-Physics-Astronomy **327**, 1015 (1999).
- 965 [38] R. Lebas, T. Menard, P. A. Beau, A. Berlemont, and F. X. Demoulin, *Numerical Simulation of*
966 *Primary Break-up and Atomization: DNS and Modelling Study*, Int. J. Multiph. Flow **35**, 247
967 (2009).
- 968 [39] M. Ishii and K. Mishima, *Two-Fluid Model and Hydrodynamic Constitutive Relations*, Nucl.
969 Eng. Des. **82**, 107 (1984).
- 970 [40] J. Boussinesq, *Essai Sur La Théorie Des Eaux Courantes*, Mémoires Présentés Par Divers
971 Savants à l'Académie Des Sci. **23**, 1 (1877).
- 972 [41] J. U. Brackbill, D. B. Kothe, and C. Zemach, *A Continuum Method for Modeling Surface*
973 *Tension*, J. Comput. Phys. **100**, 335 (1992).
- 974 [42] G. I. Kelbaliyev, *Drag Coefficients of Various Shaped Solid Particles, Drops, and Bubbles*,
975 Theor. Found. Chem. Eng. **45**, 248 (2011).
- 976 [43] A. Vallet, A. A. Burluka, and R. Borghi, *Development of a Eulerian Model for the "Atomization"*
977 *of a Liquid Jet*, At. Sprays **11**, (2001).
- 978 [44] A. Andreini, C. Bianchini, S. Puggelli, and F. X. Demoulin, *Development of a Turbulent Liquid*
979 *Flux Model for Eulerian-Eulerian Multiphase Flow Simulations*, Int. J. Multiph. Flow **81**, 88
980 (2016).
- 981 [45] J. Chesnel, J. Reveillon, T. Menard, and F. X. Demoulin, *Large Eddy Simulation of Liquid Jet*
982 *Atomization*, At. Sprays **21**, 711 (2011).
- 983 [46] G. Nykteri and M. Gavaises, *Droplet Aerobreakup under the Shear-Induced Entrainment*
984 *Regime Using a Multiscale Two-Fluid Approach*, Phys. Rev. Fluids **6**, 084304 (2021).
- 985 [47] M. J. Iving, D. M. Causon, and E. F. Toro, *On Riemann Solvers for Compressible Liquids*, Int. J.
986 Numer. Methods Fluids **28**, 395 (1998).
- 987 [48] R. T. Lahey, *The Simulation of Multidimensional Multiphase Flows*, Nucl. Eng. Des. **235**, 1043
988 (2005).
- 989 [49] S. Karthika, T. K. Radhakrishnan, and P. Kalaichelvi, *A Review of Classical and Nonclassical*
990 *Nucleation Theories*, Cryst. Growth Des. **16**, 6663 (2016).
- 991 [50] E. Villermaux and B. Bossa, *Drop Fragmentation on Impact*, J. Fluid Mech. **668**, 412 (2011).
- 992 [51] V. S. Jagadale, D. C. K. Rao, D. Deshmukh, D. Hanstorp, and Y. N. Mishra, *Modes of*
993 *Atomization in Biofuel Droplets Induced by a Focused Laser Pulse*, Fuel **315**, 123190 (2022).
- 994 [52] P. Sopeña, J. M. Fernández-Pradas, and P. Serra, *Laser-Induced Forward Transfer of*
995 *Conductive Screen-Printing Inks*, Appl. Surf. Sci. **507**, (2020).
- 996 [53] J. Zhou and M. Andersson, *Break-up Induced by the Collapse of Laser-Generated Cavitation*
997 *Bubbles in a Liquid Jet*, 1 (2018).
- 998 [54] P. Rohilla and J. Marston, *Feasibility of Laser Induced Jets in Needle Free Jet Injections*, Int. J.
999 Pharm. **589**, 119714 (2020).
- 1000 [55] Y. Guo, Y. Lian, and M. Sussman, *Investigation of Drop Impact on Dry and Wet Surfaces with*
1001 *Consideration of Surrounding Air*, Phys. Fluids **28**, (2016).
- 1002 [56] N. Kyriazis, P. Koukouvinis, and M. Gavaises, *Modelling Cavitation during Drop Impact on*
1003 *Solid Surfaces*, Adv. Colloid Interface Sci. **260**, 46 (2018).

1004 [57] Y. Wang, R. Dandekar, N. Bustos, S. Poulain, and L. Bourouiba, *Universal Rim Thickness in*
1005 *Unsteady Sheet Fragmentation*, Phys. Rev. Lett. **120**, 204503 (2018).
1006